

Robust Solid Boundary Treatment for Compressible Smoothed Particle Hydrodynamics

Navaneet Villodi^{1, a)} and Prabhu Ramachandran^{1, b)}

*Department of Aerospace Engineering, Indian Institute of Technology Bombay,
Powai, Mumbai 400076*

(Dated: 27 August 2024)

The unavailability of accurate boundary treatment methods for compressible Smoothed Particle Hydrodynamics (SPH) severely limits its ability to simulate flows in and around bodies. To this end, challenges specific to compressible flows with SPH are carefully considered. Based on these, robust and widely applicable boundary treatment methods for compressible SPH are proposed. These are accompanied by a novel technique to prevent particle penetration at boundaries. The proposed methods are shown to be significantly better than other recent approaches. A wide variety of test problems, many of which are not shown to be simulated with SPH thus far, are employed to highlight the strengths and weaknesses of the proposed methods. The implementation is open source and the results are automated in the interest of reproducibility. Overall, this research contributes to the advancement of SPH as a viable alternative to mesh-based methods for compressible flow simulations.

^{a)}Corresponding Author: navaneet@iitb.ac.in

^{b)}prabhu@aero.iitb.ac.in; <http://www.aero.iitb.ac.in/~prabhu>

I. INTRODUCTION

Smoothed Particle Hydrodynamics (SPH) is quite capable of simulating compressible fluid flows and has been widely used for simulating various phenomena involving compressible hydrodynamics^{1,2}. Many applications usually involve flow in and around bodies. To simulate these, proper boundary treatment methods are required to accurately model the physics at the boundary.

The boundaries that need to be dealt with can be broadly classified into two categories: permeable boundaries and solid wall boundaries. Permeable boundaries are those that allow fluid to enter or exit the computational domain. Permeable boundary treatment methods for incompressible flows should not pose major setbacks for use with compressible flows. Solid wall boundaries are commonly dealt with using ghost particles³⁻¹¹. All of these have been proposed for incompressible and weakly compressible flows. The solid wall boundary treatment methods proposed in the incompressible and weakly compressible SPH literature do not work well for compressible flows. The following are the major issues that remain unresolved in the context of compressible flows and are addressed in this work:

1. Particle penetration: Compressible flows result in scenarios that encourage particles to creep into the boundary. Popular methods from the incompressible SPH literature like that of Adami *et al.*⁹ suffer from this (see fig. 2a). A detailed discussion on the reasons behind this is presented in section III E.
2. Inaccuracies: Particle penetration brings with it inaccuracies and instabilities. The use of short-range repulsive forces is effective in avoiding particle penetration^{12,13}. However, these results also leave much to be desired. The methods presented in the present work furnish demonstrably better results (see table I).
3. Lack of simulation data: There is limited simulation data available for compressible flows with solid boundaries using SPH as most of the compressible flow test cases and benchmark problems that are used to validate SPH schemes are without solid wall boundaries. The work of Sun *et al.*¹⁴ showcases some interesting simulations involving compressible flows with boundaries. They claim to have used the method of Marrone *et al.*⁸. As this method was introduced to be used with incompressible flows, we found the details regarding modifications, if any, to be missing. Moreover,

their problems do not focus on shocks and shock-boundary interactions. The present work includes a wide variety of problems including but not limited to shocks and shock-boundary interactions.

The existing boundary treatment methods in SPH are augmented with following major ideas to address the above issues:

1. Judicious extrapolation: Differently from Marrone *et al.*⁸, Adami *et al.*⁹, instead of just pressure and velocity, all relevant quantities are extrapolated from the fluid domain to the ghost particles in a manner that is consistent with the boundary conditions, as explained in section III D.
2. Ghost volume constancy: While the density of a ghost particle is allowed to vary, its volume should be constant for the ghost particles to be an effective partition of space. This improves the quality of results and curtails the particle penetration problem to a large extent. The rationale is explained in section III E 1.
3. Penetration shield: For extreme cases where the above is not sufficient, a penetration shield is introduced. The particles that are on a collision course with the boundary are steered away making use of the Transport Velocity Formulation (TVF)¹⁵, as explained in section III E 2.

The rest of this paper is organized as follows. Section II presents a detailed overview of permeable and solid boundary treatment methods in SPH. Section III lays down the governing equations and the discretization scheme used in this study. We also outline what is expected at the boundary and the boundary treatment strategy that is used in this study. Further, the challenges that are unique to the treatment of boundaries in compressible SPH are dissected. Remedial measures to address these issues are also presented therein. Section IV demonstrates that the proposed techniques are capable of simulating a diverse collection of benchmark problems. These include problems involving oblique shocks, normal shocks, bow shocks, subsonic to supersonic transition, complex wave interactions, flow over bodies with sharp edges, flow over moving bodies, and three-dimensional flows. Section V summarizes the work. Finally, section VI presents some suggestions for future and concludes the work.

II. STATE OF BOUNDARY TREATMENT METHODS

With SPH, incompressible flows are usually simulated using Weakly Compressible SPH (WCSPH) and Incompressible SPH (ISPH) schemes. A considerable amount of progress has been made in the treatment of boundary conditions with WCSPH and ISPH. The recent work of Negi and Ramachandran¹⁶, wherein the popular boundary treatment techniques have been rigorously benchmarked using Method of Manufactured Solutions (MMS), serves as a structured review of these boundary treatment methods in SPH. We also touch upon some notable boundary treatment methods in the subsequent subsections.

A. Permeable boundaries

Implementation of permeable boundaries in SPH generally involves the use of buffer zones¹⁷⁻²¹. These buffer zones facilitate the entry and exit of fluid particles. There also exist methods that do not conform to this framework^{22,23}. Werdelmann *et al.*²⁴ presents a concise summary of permeable boundary treatment methods for SPH along with their own novel framework for the same.

As far as permeable boundaries are concerned, the implementations from ISPH and WCSPH can be applied, mostly without any fundamental modifications, to compressible flow simulations. In supersonic flows, all the quantities can be set at the inlet as all characteristics at the inlet are known to be directed into the domain. Therefore, an extrapolation procedure, like that employed by Tafuni *et al.*¹⁹ is not necessary for supersonic flows.

On the account that existing permeable boundary treatment methods can be relied upon, we chose to focus on the shortcomings with the treatment of solid boundaries and make use of Federico *et al.*¹⁸'s method for permeable boundaries. This choice is motivated by the ease of implementation. We are aware of the fact that Negi and Ramachandran¹⁶ found this method to be not the most optimal method for convergence. We also do not discount the potential issues this method may pose, for instance, being ineffective when the velocity components are normal to the interface²⁴.

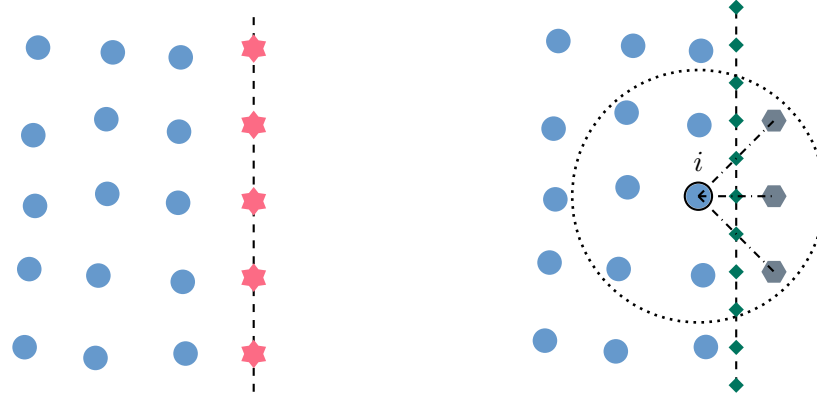
B. Solid wall boundaries

In this section, we touch upon the notable solid boundary treatment methods from the literature.

Earliest attempts to implement solid boundary conditions in SPH relied on using short-range repulsive forces^{25–27}. Fixed particles representing the boundary were conferred with the ability to exert a repulsive force on fluid particles in the vicinity. These repulsive forces could be exerted by a single layer of particles at the interface as shown in fig. 1a. Having a single layer of particles at the interface is appealing as it makes the representation of complex geometries easier, albeit at the cost of kernel truncation errors. In fact, Campbell²⁸ had emphasized the retention of boundary integral or wall normalization terms while deriving the discretized governing equations to remedy the errors due to kernel truncation when a single layer of particles is used. The discretionary nature of the form of force that is employed is another notable disadvantage of this approach. The methods of Marongiu *et al.*²⁹, Hashemi *et al.*³⁰ are some other notable methods that employ a single layer of particles at the interface. As expected, these methods exhibit poor convergence¹⁶.

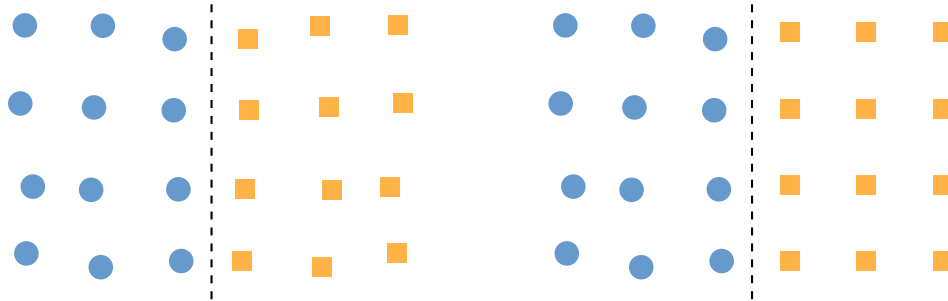
The semi-analytical boundary treatment method of Kulasegaram *et al.*³¹ has its governing equations derived from a variational formulation with wall renormalization terms incorporated. Therefore, additional correction factors appear in their equations. These correction factors were computed using a polynomial approximation. Later, Feldman and Bonet³² showed that the correction factors can be computed exactly. Kulasegaram *et al.*³¹'s approximation was found to be in good agreement with the exact values computed by Feldman and Bonet³². Subsequently, Ferrand *et al.*³³ laid out a better way to compute and evolve these correction factors in-simulation. Semi-analytical boundary treatment methods have been under development ever since^{34–38}. They have also been extended to open boundaries^{23,39}. Nonetheless, they have not yet garnered the widespread adoption that ghost particle based methods enjoy.

The work of Takeda *et al.*³ is one of the early endeavors to impose a no-slip condition that explored the use of mirrored ghost particles, i.e., ghost particles generated by mirroring fluid particles about the interface as depicted in fig. 1c. However, their approach is challenging to implement for complex non-planar interfaces. Later, Morris *et al.*⁴ introduced a method that places all the particles on a regular lattice throughout the computational domain and



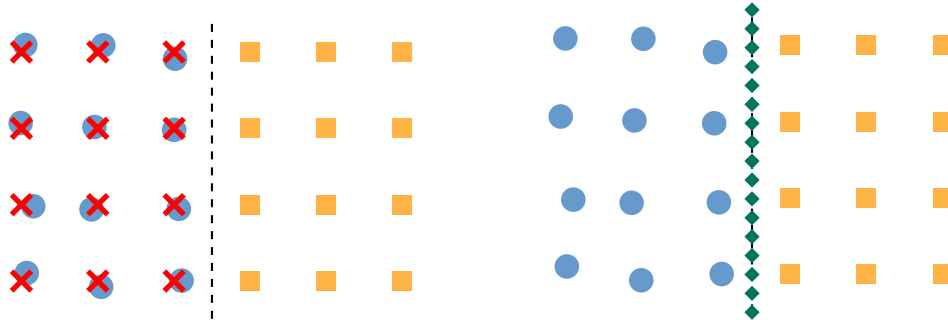
(a)

(b)



(c)

(d)



(e)

(f)

FIG. 1. Various particle arrangements at the boundary interface. (a) Boundary represented by a single layer of fixed particles at the interface. (b) Boundary treatment using fictitious and inert particles. Fictitious particles generated for a fluid particle i are shown. The region of dependence is marked by the dotted circle. (c) Ghost particles mirroring fluid particles about the interface. (d) Ghost particles which are stationary with respect to the interface. (e) Ghost particles which are stationary with respect to the interface paired with accomplices which mirror them about the interface. (f) Ghost particles which are stationary with respect to the interface and inert particles at the interface.

designates the particles that fall within a solid object as ghost particles. Morris *et al.*⁴'s method borrowed Takeda *et al.*³'s approach for estimating ghost particles' velocity for no-slip. This method makes representing interfaces less complicated at the cost of imperfect representation of curved boundaries. Since the ghost particles of Takeda *et al.*³ and Morris *et al.*⁴ do not inherit the pressure and density of their fluid counterparts, the accuracy of the pressure gradient near the boundary is expected to be inaccurate. Unlike them, Colagrossi and Landrini⁵ made use of mirrored ghost particles that inherit the pressure and density of their fluid counterparts to impose the free-slip condition. Subsequently, Yildiz *et al.*⁶ employed mirrored ghost particles to impose a no-slip condition, also highlighting some limitations of Morris *et al.*⁴'s method and attempting to improve those. Nevertheless, their technique also sticks out as rather elaborate and onerous to implement. Later, Macia *et al.*⁷ came up with a consistent formulation for the Laplacian operator as an extension to Takeda *et al.*³'s work. This corrected formulation was seminal for the implementation of the no-slip boundary condition.

Ferrari *et al.*⁴⁰ introduced a new boundary treatment method that makes use of virtual particles generated by locally mirroring fluid particles about points located on the interface, as shown in fig. 1b. These virtual or fictitious particles are generated for each particle near the boundary and are not shared, i.e. one fluid particle cannot access another fluid particle's virtual particles. Since the points or particles situated on the interface are present only to act as local points of symmetry for the generation of fictitious particles and do not interact with the fluid particles, they can be termed inert. Vacondio *et al.*⁴¹ improved Ferrari *et al.*⁴⁰'s method by enabling an additional layer of virtual particles and introducing better treatment of corners. Fourtakas *et al.*⁴² introduced further enhancements to the fictitious particle generation algorithm, mainly focussing on ensuring better support for the fluid particles. Recently, Fourtakas *et al.*⁴³ introduced a new method in which they discarded the use of inert particles altogether in favor of using triangles to discretise the boundary interfaces. They also replaced locally mirrored particles with a Local Uniform STencil (LUST) of fictitious particles that surround every particle. The particles in LUST that are located within the fluid domain are turned off while the contributions from the rest are used.

Dynamic Boundary Condition (DBC) consider multiple layers of ghost particles to model the solid boundaries, as shown in fig. 1d. The density at the ghost particle is updated

using summation density. With this density, Crespo *et al.*⁴⁴ shows that the pressure at the ghost particle can be evaluated using the first term from the Taylor expansion of the equation of state. This pressure acts naturally through the pressure gradient term in the momentum equation to influence the acceleration of the interacting fluid particle. As we understand, computing pressure this way, compared to using the actual equation lends a marginal reduction of computational effort.

The ghost particles that are used in this case do not mirror a fluid particle about the interface. They remain stationary unless they represent a moving boundary. Utilizing this property, Ren *et al.*⁴⁵ show that dynamic boundary conditions can be used for fluid-rigid body coupling problems just like Akinci *et al.*⁴⁶, Liu *et al.*⁴⁷. Later, Li *et al.*⁴⁸ contended that the particle penetration problem with Crespo *et al.*⁴⁴'s approach can be addressed by enhancing the forces between fluid particles and boundary particles. They proposed a procedure to improve the uniformity of the repulsive forces and recommended employing a higher-order expansion of the equation of state for this. Recently, English *et al.*⁴⁹ presented a method which they named as modified DBC (mDBC). Their setup is akin to that used by Marrone *et al.*^{8,10}, as depicted in fig. 1e and explained later in section III D, with the difference that they extrapolate only the density from ghost-mirror to ghost. The actual equation of state is used to compute the pressure. They demonstrate that their method results in a hydrostatic pressure that is less noisy compared to the former DBC. However, we note that their method targets the Neumann boundary condition for density about the interface instead of the Neumann boundary condition for pressure.

Non-homogenous Neumann boundary conditions are being actively explored, especially for heat transfer simulations. For example, Sikarudi and Nikseresht⁵⁰ explored two methods of implementing non-homogenous Neumann boundary conditions without ghost particles. The work of Wang *et al.*⁵¹ is another example where they demonstrated three ways to treat non-homogenous Neumann boundary conditions making use of ghost particles.

It is clear that most methods make use of ghost particles in some form or other. Of these, the technique of Adami *et al.*⁹ has garnered wide adoption. Valizadeh and Monaghan⁵² studied and compared variations of Monaghan and Kajtar²⁷'s and Adami *et al.*⁹'s methods with a host of test problems. Their results declare Adami *et al.*⁹'s method as the better one. On the other hand, the study by Negi and Ramachandran¹⁶ reveals that the solid boundary treatment method of Marrone *et al.*⁸ yields better convergence. As noted earlier, most of

these boundary treatment methods have been employed in the context of incompressible or weakly compressible SPH. The present work seeks to identify suitable methods for compressible fluid flow problems. The approach employed in this paper is based on these two methods. We present the details in section III D, but before that we need to introduce the basic discretization that is used in this study.

III. FORMULATION

A. Governing equations

Inviscid compressible flow is governed by the Euler equations, which are given as,

$$\frac{d\rho}{dt} = -\rho \nabla \cdot \mathbf{u}, \quad (1)$$

$$\frac{d\mathbf{u}}{dt} = -\frac{1}{\rho} \nabla p, \quad (2)$$

$$\frac{de}{dt} = -\frac{p}{\rho} \nabla \cdot \mathbf{u}. \quad (3)$$

Here, d/dt represents the material derivative, ρ is the density, p is the pressure, \mathbf{u} is the velocity, and e is the thermal energy per unit mass.

With the ideal gas assumption, this system is closed with an equation of state,

$$p = (\gamma - 1)\rho e, \quad (4)$$

where γ is the ratio of the specific heat of the gas at constant pressure to its specific heat at constant volume. γ is constant for a calorifically perfect gas.

B. Semi-discretised governing equations

We assume readers' familiarity with the basics of SPH discretization and proceed to list out the discretized form of the above equations as per the compressible δ -SPH scheme of Sun *et al.*¹⁴. These discretized equations also contain additional stabilizing terms. It may be noted that there was no particular motivation behind the selection of the compressible δ -SPH scheme as the base for this study. We also see no reason for any other compressible scheme to not work with the proposed boundary treatment explained in further sections.

The δ -SPH makes use of renormalized kernel gradients, introduced by Randles and Libersky⁵³, and employs an anti-symmetric, conservative discretization for the gradient of pressure and a symmetric, non-conservative discretization for the divergence of velocity. If \mathcal{N}_i be the set of particles in the neighborhood of a particle, indexed i , the divergence velocity, $\nabla \cdot \mathbf{u}$, at i is expressed as a summation over its neighbor particles, $\{j : j \in \mathcal{N}_i\}$, as

$$\langle \nabla \cdot \mathbf{u} \rangle_i^L = \sum_j (\mathbf{u}_j - \mathbf{u}_i) \cdot \nabla_i W_{ij}^C \frac{m_j}{\rho_j}, \quad (5)$$

where

$$\nabla_i W_{ij}^C = \mathbb{L}_i \nabla_i W_{ij}, \quad (6)$$

$$\mathbb{L}_i = \left[\sum_k (\mathbf{r}_j - \mathbf{r}_k) \otimes \nabla_i W_{ik} \frac{m_k}{\rho_k} \right]^{-1}. \quad (7)$$

Here, W_{ij} is a shorthand for the SPH kernel, $W(|\mathbf{r}_i - \mathbf{r}_j|, h_{ij})$; \mathbf{r} is used to represent position vectors; \otimes represents the outer product; h is the smoothing length; and $h_{ij} = (h_i + h_j)/2$.

Similarly, the gradient of a general scalar variable f may be expressed as

$$\langle \nabla f \rangle_i^L = \sum_j (f_j - f_i) \nabla_i W_{ij}^C \frac{m_j}{\rho_j}. \quad (8)$$

However, the following anti-symmetric approach is used for the gradient of pressure,

$$\langle \nabla f \rangle_i^{L2} = \sum_j (f_i \nabla_i W_{ij}^C - f_j \nabla_j W_{ij}^C) \frac{m_j}{\rho_j}, \quad (9)$$

Equation (9) is used to compute the gradient of pressure. The superscripts L and $L2$ are merely labels to distinguish between the two gradient operators.

Now, the discretized counterpart of continuity equation (1), along with an additional diffusion term reads

$$\frac{d\rho_i}{dt} = -\rho_i \langle \nabla \cdot \mathbf{u} \rangle_i^L + \delta \sum_j \phi_{ij} c_{ij} h_{ij} \mathcal{D}_{ij} \cdot \nabla_i W_{ij} \frac{m_j}{\rho_j}. \quad (10)$$

Here, the second term on the RHS imparts diffusion for density. δ is set as 0.1, as proposed by Antuono *et al.*⁵⁴. The parameter ϕ_{ij} is set as 1 if the interacting phases are the same, else 0. c is the speed of sound, computed as $c_i = \sqrt{\gamma p_i / \rho_i}$ and symmetrised as $c_{ij} = (c_i + c_j)/2$. \mathcal{D}_{ij} is given as

$$\mathcal{D}_{ij} = \frac{2\mathbf{r}_{ji}}{\|\mathbf{r}_{ji}\|^2} \left[(\rho_j - \rho_i) - \frac{1}{2} (\langle \nabla \rho \rangle_i^L + \langle \nabla \rho \rangle_j^L) \cdot \mathbf{r}_{ji} \right], \quad (11)$$

where $\mathbf{r}_{ij} = \mathbf{r}_i - \mathbf{r}_j = -\mathbf{r}_{ji}$. Instead of eq. (10), one may also use summation density with an iterative solution for smoothing lengths just like Price⁵⁵, Puri and Ramachandran⁵⁶.

Similar to the continuity equation, the discretized counterpart of momentum equation (2), with an additional artificial viscosity term reads

$$\frac{d\mathbf{u}_i}{dt} = -\frac{1}{\rho_i} \langle \nabla p \rangle_i^{L2} + \sum_j \frac{\rho_j}{\rho_{ij}} \Pi_{ij} \nabla_i W_{ij} \frac{m_j}{\rho_j}, \quad (12)$$

where

$$\Pi_{ij} = \alpha c_{ij} \frac{h_{ij} \mathbf{u}_{ij} \cdot \mathbf{r}_{ij}}{\|\mathbf{r}_{ij}\|^2} - \beta \left(\frac{h_{ij} \mathbf{u}_{ij} \cdot \mathbf{r}_{ij}}{\|\mathbf{r}_{ij}\|^2} \right)^2 \text{ if } \mathbf{u}_{ij} \cdot \mathbf{r}_{ij} < 0 \text{ else } 0. \quad (13)$$

Here, $\rho_{ij} = (\rho_i + \rho_j)/2$ and $\mathbf{u}_{ij} = \mathbf{u}_i - \mathbf{u}_j$. The parameters α and β are set as 1 and 2 respectively.

Finally, the discretized counterpart of energy equation (3), with the additional artificial viscosity term and an additional artificial conduction term may be expressed as

$$\begin{aligned} \frac{de_i}{dt} = & -\frac{p_i}{\rho_i} \langle \nabla \cdot \mathbf{u} \rangle_i^L - \frac{1}{2} \sum_j \frac{\rho_j}{\rho_{ij}} \Pi_{ij} \mathbf{u}_{ij} \cdot \nabla_i W_{ij} \frac{m_j}{\rho_j} \\ & + \kappa \sum_j \phi_{ij} c_{ij} h_{ij} \mathcal{E}_{ij} \cdot \nabla_i W_{ij} \frac{m_j}{\rho_j}. \end{aligned} \quad (14)$$

Here, the second term on the RHS encapsulates the contribution of artificial viscosity. The third term is the artificial conduction term. κ is a constant set as 0.1. \mathcal{E}_{ij} is given as

$$\mathcal{E}_{ij} = 2(e_j - e_i) \mathbf{r}_{ji} / \|\mathbf{r}_{ji}\|^2. \quad (15)$$

The equation of state is straightforwardly discretized as

$$p_i = (\gamma - 1) \rho_i e_i. \quad (16)$$

When the continuity equation(10) is used to update density, smoothing length is updated using,

$$\frac{dh}{dt} = -\frac{h}{d \cdot \rho} \frac{d\rho}{dt}, \quad (17)$$

Here, d can be 1, 2, or 3 depending upon whether the problem is one, two or three-dimensional, respectively.

C. TVF

The particles can be moved with a transport velocity, $\tilde{\mathbf{u}}$ which is different from the Lagrangian velocity, \mathbf{u} by making use of the TVF formulation. We refer the readers to the work of Sun *et al.*⁵⁷ for more details and to the work of Adepur and Ramachandran⁵⁸ for a detailed derivation. The gist is that if we define

$$\delta\mathbf{u} = \mathbf{u} - \tilde{\mathbf{u}}, \quad (18)$$

then the accelerations in eqs. (10), (12) and (14) can practically be expressed incorporating transport velocity as

$$\begin{aligned} \frac{\tilde{d}\rho_i}{dt} &= -\rho_i \langle \nabla \cdot \mathbf{u} \rangle_i^L - \rho_i \langle \nabla \cdot \delta\mathbf{u} \rangle_i + \langle \nabla \cdot (\rho\delta\mathbf{u}) \rangle_i \\ &\quad + \delta \sum_j \phi_{ij} c_{ij} h_{ij} \mathcal{D}_{ij} \cdot \nabla_i W_{ij} \frac{m_j}{\rho_j}, \end{aligned} \quad (19)$$

$$\begin{aligned} \frac{\tilde{d}\mathbf{u}_i}{dt} &= -\frac{1}{\rho_i} \langle \nabla p \rangle_i^{L2} + \rho_i \langle \nabla \cdot (\mathbf{u} \otimes \delta\mathbf{u}) \rangle_i - \rho_i \mathbf{u}_i \langle \nabla \cdot \delta\mathbf{u} \rangle_i \\ &\quad + \sum_j \frac{\rho_j}{\rho_{ij}} \Pi_{ij} \nabla_i W_{ij} \frac{m_j}{\rho_j}, \end{aligned} \quad (20)$$

and

$$\begin{aligned} \frac{\tilde{d}e_i}{dt} &= -\frac{p_i}{\rho_i} \langle \nabla \cdot \mathbf{u} \rangle_i^L - e_i \langle \nabla \cdot \delta\mathbf{u} \rangle_i + \langle \nabla \cdot (e\delta\mathbf{u}) \rangle_i \\ &\quad - \frac{1}{2} \sum_j \frac{\rho_j}{\rho_{ij}} \Pi_{ij} \mathbf{u}_{ij} \cdot \nabla_i W_{ij} \frac{m_j}{\rho_j} \\ &\quad + \kappa \sum_j \phi_{ij} c_{ij} h_{ij} \mathcal{E}_{ij} \cdot \nabla_i W_{ij} \frac{m_j}{\rho_j}, \end{aligned} \quad (21)$$

where

$$\langle \nabla \cdot (f\delta\mathbf{u}) \rangle_i = \sum_j (f_j \delta\mathbf{u}_j + f_i \delta\mathbf{u}_i) \cdot \nabla_i W_{ij} \frac{m_j}{\rho_j}, \quad (22)$$

and

$$\langle \nabla \cdot (\mathbf{u} \otimes \delta\mathbf{u}) \rangle_i = \sum_j (\mathbf{u}_j \otimes \delta\mathbf{u}_j + \mathbf{u}_i \otimes \delta\mathbf{u}_i) \cdot \nabla_i W_{ij} \frac{m_j}{\rho_j}. \quad (23)$$

Here, \tilde{d}/dt represents the material derivative with respect to the transport velocity. It can be easily noted that when $\delta\mathbf{u} = 0$, then eqs. (19) to (21) reduce to eqs. (10), (12) and (14), respectively.

We make use of TVF in the penetration shield that is proposed ahead. The TVF also finds use in particle shifting. Essentially, the shifting velocity is embodied as a transport velocity. While shifting techniques regularise particle distributions, it is also found that shifting does not play well with the shocks. One could use a shock detector⁵⁹⁻⁶² and avoid shifting near the shocks or try more sophisticated shifting algorithms^{63,64}, however, we mark this as a subject for future work and stick with boundary treatment methods for now.

D. Boundary Treatment Strategy

In the case of inviscid flows, we are aiming for a free-slip and no-penetration boundary condition. This entails that the fluid particles in the immediate vicinity of the interface should have a velocity that is tangential to the interface and the pressure Neumann condition is to be satisfied at the interface. These can be achieved by setting the velocities and pressures of the ghost particles such that they mirror the component of velocity normal to the interface and the pressure of the fluid particles, about the interface. This is done in two steps:

1. *Extrapolation*

The properties \mathbf{u} , e , p , and h are extrapolated from fluid to ghost. If α is variable, that is also extrapolated. We consider two approaches for this:

1. *Without ghost-mirror particles*: This is based on method of Adami *et al.*⁹. This approach relies on interpolation to extrapolate properties from fluid to ghost particles. We will let eq. (24) clarify this seemingly paradoxical statement. The ghost particles are placed across the prescribed boundary as shown in fig. 1d. To extrapolate a property f from fluid to ghost particles, the following expression is evaluated

$$f_i = \frac{\sum_j f_j W_{ij}}{\sum_j W_{ij}}. \quad (24)$$

In this expression, i represents ghost particles and j represents fluid particles in the neighborhood of the corresponding ghost particle. So, the summation is over the neighboring fluid particles instead of all the neighboring particles. Adami *et al.*⁹ recommends using the equation of state to obtain density with the extrapolated properties.

Others are able to get good results by obtaining density using summation density^{65–67} for the solid particles. In the present study, we stick with the former approach. In plots hereafter, this variant is abbreviated as WOM.

2. *With ghost-mirror particles*: This is based on the method of Marrone *et al.*⁸. In this approach, the ghost particles are placed across the prescribed boundary. Another set of particles is placed in the fluid region mirroring the location of the ghost particles about the boundary, as shown in fig. 1e. These are the ghost-mirror particles. Fluid particles interact with ghost particles but not with ghost-mirror particles. The ghost-mirror particles exist for the sole purpose of interpolation of properties. The properties are interpolated using a Moving Least Squares (MLS) interpolator. Practically, this boils down to SPH interpolation by using kernel correction of Liu and Liu⁶⁸. Thus, to extrapolate a scalar property f from fluid to ghost particles, the following expression is evaluated

$$f_i = \sum_j f_j W_{ij}^{LC} V_j. \quad (25)$$

where W_{ij}^{LC} is the kernel with the correction of Liu and Liu⁶⁸ applied. Then, these properties are copied over from ghost-mirror to the corresponding ghost particles. This variant is abbreviated as WM in plots hereafter.

2. *Post extrapolation*

The extrapolated pressure and velocity need to be modified further to ensure that the boundary conditions are enforced. Let us denote the velocity obtained by extrapolation as $\mathbf{u}_{\text{extrapolated}}$. Then, the velocity of the ghost particles is set as

$$\mathbf{u}_i = 2\mathbf{u}_{i,\text{prescribed}} - \mathbf{u}_{i,\text{extrapolated}}, \quad (26)$$

where $\mathbf{u}_{\text{prescribed}}$ is the prescribed velocity of the boundary. For free-slip, this prescribed velocity equals the velocity of the fluid tangential to the boundary. So, given the normal to the boundary $\hat{\mathbf{n}}$, the prescribed velocity is

$$\mathbf{u}_{i,\text{prescribed}} = \mathbf{u}_{i,\text{extrapolated}} - \mathbf{u}_{i,\text{extrapolated}} \cdot \hat{\mathbf{n}}_i, \quad (27)$$

In case the interface is moving with a velocity, $\mathbf{u}_{\text{interface}}$, the prescribed velocity would be

$$\mathbf{u}_{i,\text{prescribed}} = \mathbf{u}_{i,\text{interface}} + \mathbf{u}_{i,\text{extrapolated}} - \mathbf{u}_{i,\text{extrapolated}} \cdot \hat{\mathbf{n}}_i, \quad (28)$$

The extrapolation of pressure onto ghosts aims at ensuring that the pressure gradient normal to the interface is zero, i.e., $\partial p/\partial n = 0$. However, this condition is valid only when there are no body forces and the interface is not accelerating. We consider the body forces to be zero. For accelerating interfaces, this needs to be adjusted to ensure that the pressure conferred by the ghost particles on fluid particles is consistent with the acceleration of the interface. This is done by setting the pressure of the ghost particles as

$$p_i = p_{i,\text{extrapolated}} + 2\Delta s_{i,g2i} \left. \frac{\partial p}{\partial n} \right|_i, \quad (29)$$

where Δs_{g2i} is the distance to the interface. Exploiting eq. (2), $\partial p/\partial n$ may be estimated as,

$$\left. \frac{\partial p}{\partial n} \right|_i = -\rho_i \mathbf{a}_i \cdot \hat{\mathbf{n}}_i. \quad (30)$$

where $\mathbf{a} = d\mathbf{u}/dt$ is the acceleration of the ghost particle representing the accelerating interface. While Marrone *et al.*⁸ does not consider accelerating interfaces, Adami *et al.*⁹, Antuono *et al.*¹¹ do include similar terms to account for the acceleration of the interface. This concludes our description of the general strategy for the treatment of solid boundaries.

E. The challenges and remedies

The fluid and ghost particles are initialized with some spacing following the prescribed mass and density. The particle density and the fluid density are related. In fact, if a constant mass discretization is assumed, the particle density is solely responsible for representing fluid density. Given that the density of a fluid parcel is expected to not change significantly as it moves with the flow velocity in incompressible flows, the average spacing between the fluid particles is expected to be fairly constant. Therefore, in incompressible flows, if the ghost particles and fluid particles that interact are set up well, they do not end up in a situation where the fluid particles are spaced much closer than the ghost particles or vice-versa. Even if adaptive resolution is employed, the particle spacing is varied smoothly^{66,67,69,70}. However, the density can vary significantly in compressible flows and so can the spacing. As a result, scenarios that may result in a substantial difference in spacing at the interface may evolve. This promotes interpolation errors.

Furthermore, the local average particle spacing, Δs_{avg} , is expected to be consistent with the effective volume associated with the particle,

$$m/\rho \propto (\Delta s_{\text{avg}})^d. \quad (31)$$

The density of the ghost particles may be computed using summation density, or using the equation of state after its pressure and energy are set. Either way, a change in density invariably changes the effective volume associated with the ghost particle. This volume may turn out to be inconsistent with the actual particle spacing. In other words, the ghost particles end up being an ineffective partition of space altogether.

The equation of state plays an interesting role in the repulsion mechanism that is described by many authors^{44,49}. In WCSPH, when particles come closer and density increases, the pressure increase is manifold. This transpires by virtue of the stiff equation of the state that is used in WCSPH. Consequently, a repulsion is generated via the pressure term in the momentum equation. This repulsion curtails the tendency of fluid particles to leak through the ghost particles. For instance, leakage can be observed in the simulation of 3D dam break using Simple Iterative SPH (SISPH)⁷¹, a derivative of ISPH but not with Entropically Damped Artificial Compressibility (EDAC)-SPH or Dual-Time SPH (DTSPH)⁷², both of which are WCSPH derivatives. The pressure and density are linearly related in ideal gas equation of state that is commonly used with compressible SPH. Therefore, this repulsion is rather inconsequential. This repulsion deficiency may be compensated by increasing artificial viscosity and using particle shifting techniques. We also need to be mindful of the fact that neither of these is free of consequences.

Careful consideration of the above-described idiosyncrasies regarding compressible flows with boundaries in SPH equipped us to direct our efforts into mitigating these. Based on our investigations, we propose the following remedies, which are simple yet effective in addressing the issues described above.

1. Ghost volume constancy

The effective volume $V = m/\rho$ of the ghost particles must be maintained constant. This is in line with the idea that the ghost particles represent a partition of space and if they do not move, there is no reason for their volume to change. Upon density change, one may ensure volume constancy by resetting the mass of the ghost particle accordingly. It may also be noted from the equations in section III that m and ρ always occur as m/ρ inside the summation, except for the ρ in artificial viscosity and density diffusion terms. Therefore, it would suffice if the ghost particles do not have an explicit mass property m as long as they

have a constant volume property V and a density property ρ .

2. Penetration shield

While maintaining the effective volume of the ghost particles constant is enough for most cases, it is not foolproof as there may be cases where one cannot predict how the flow field will evolve. There is still a risk of fluid particles ending up interacting with ghost particles with wildly different associated volumes and leaking through. For such situations, we propose a penetration shield. In this procedure, a fluid particle that is on a course to penetrate the interface is steered away using transport velocity as

$$\delta \mathbf{u}_i = \delta u_i \hat{\mathbf{n}}_{i,\text{in}} \quad (32)$$

where

$$\delta u_i = \begin{cases} 2.0 \frac{\Delta s_{i,\text{nom}} - \Delta s_{i,\text{f2g}}}{\Delta s_{i,\text{nom}}} \hat{\mathbf{n}}_{i,\text{in}} \cdot \mathbf{u}_i & \text{if } \hat{\mathbf{n}}_{i,\text{in}} \cdot \mathbf{u}_i < 0 \text{ and } \Delta s_{i,\text{f2g}} < \Delta s_{i,\text{nom}} \\ 0 & \text{otherwise} \end{cases} \quad (33)$$

Here, Δs_{nom} is the nominal spacing set as $(m/\rho)^d$, Δs_{f2g} is the distance to the nearest ghost, and $\hat{\mathbf{n}}_{\text{in}}$ represents a unit vector that is normal to the interface. $\hat{\mathbf{n}}_{\text{in}}$ for a fluid particle is updated by SPH interpolation of the normals carried by ghost particles. $-\hat{\mathbf{n}}_{\text{in}}$ would be pointing towards interface from the fluid side.

It is worth mentioning that this penetration shield is an elegant way to address the problem of penetration without resorting to the usage of short-range repulsive forces near the interface. It may also be noted the penetration shield is like a fallback for cases where the volume constancy is not sufficient, like in the case of extreme compressions or rarefactions. This shield actively prevents penetration in the biconvex aerofoil case presented in section IV G.

F. Time stepping and other parameters

Equations (19) to (21) are integrated in time using the Evaluate Predict Evaluate Correct (EPEC) integrator⁶⁵. The time step is computed as

$$\Delta t = C_{\text{CFL}} \min(\Delta t_{\text{vel}}, \Delta t_{\text{force}}), \quad (34)$$

where

$$\Delta t_{\text{vel}} = \frac{h_{\text{min}}}{\max(c)}, \quad (35)$$

$$\Delta t_{\text{force}} = C_{\text{force}} \sqrt{\frac{h_{\text{min}}}{\max\left(\left|\frac{d\mathbf{u}}{dt}\right|\right)}}. \quad (36)$$

C_{CFL} and C_{force} are constants, both set as 0.5.

Respecting the findings of Negi and Ramachandran¹⁶, the Quintic Spline kernel is used for all the simulations in this study. The smoothing length is set as 1.5 times the particle spacing for all problems. We found that reducing this value to 1.2 makes some of the results noisy. A fluid with $\gamma = 1.4$ is used for all problems, unless explicitly mentioned otherwise. The SPH results shown in section IV were simulated using PySPH⁷³. The ghost particles representing the bodies in the hypersonic cylinder (section IV C), biconvex aerofoil (section IV G), rotating square projectile (section IV H), and Apollo reentry capsule 3D (section IV I) problems were created using the particle packing algorithm of Negi and Ramachandran⁷⁴. The simulations were orchestrated using automan⁷⁵. In the interest of reproducibility, all the code for the present study is available at <https://gitlab.com/pypr/compressible-sph-bc>.

IV. RESULTS

A. Compression Corner

This verification case involves the computation of the supersonic flow field past a wedge. Figure 2 depicts the flow-fields over a wedge of half-angle 20° at Mach $M = 2.5$ as simulated using different approaches.

In the case of SPH, the particles at the inlet are spaced 0.0625 m apart. The meshes for the Finite Volume Method (FVM) cases were also created with comparable cell sizes. The simulation is run until $t = 10$ s. Figure 2a is the result of using our implementation of the original unmodified method of Adami *et al.*⁹. In this case, it can be seen that particles leak through the wall. In fig. 2b the result of a simple FVM implementation using First Order Upwind (FOU) scheme with approximate Riemann solver of Roe⁷⁶. It can be seen that the smearing of the shock wave increases with the distance from the corner, as expected from a first-order scheme. Figure 2c is a result of simulation with Eilmer⁷⁷. The mesh was created with Eilmer’s geometry package. This result appears comparable to the presented SPH

results. Figure 2d is a result of simulation with SU2⁷⁸. The mesh used by SU2 was created using Gmsh⁷⁹. SU2 is FVM based but it uses a cell-vertex scheme and outputs results as point data. So, a scatter plot is used for SU2 results just like the SPH cases. It can be observed that the shock is less smeared in the case of SU2 but overshoot and dispersion wiggles can also be seen.

Figure 2e and fig. 2f are the result of simulations using the methods proposed in this paper. There is no leakage of particles through the wall in either of these cases. The shock wave is more smeared than fig. 2d but the smearing does not visibly increase with distance from the corner as seen in fig. 2b. The overshoot is also more subdued than that of the other cases. The same is better quantified in fig. 3. Note that the cell data is plotted as a piecewise constant over the cell, in this figure.

For the purpose of comparison with Englestad and Cassibry¹³, the shock angle, β needs to be extracted. This is carried out by exploiting the variation of density across the shock. The gradient of density is estimated using eq. (9). The particles near the shock can be identified if their density gradient magnitude is close to the maximum density gradient within the domain. The condition

$$|\langle \nabla \rho \rangle_i| > 0.6 \max_i (|\langle \nabla \rho \rangle_i|) \quad (37)$$

is used to mark the particles near the shock. We find that the factor of 0.6 works well. The wave angle is computed from the slope of the least squares 1st order polynomial fit to these points. Comparison of error in wave angle for different configurations of compression corner problem is presented in table I. For these results, the particle spacing is matched with Englestad and Cassibry¹³ to keep the comparison fair. It can be observed that errors are consistently below 1% and considerably lower than obtained reported by Englestad and Cassibry¹³.

B. Reflecting Shocktube

This case involves the reflection of a moving normal shock from the wall. The considered domain for the shock tube is 1 m long and 0.02 m wide. The initial particle spacing is 0.002 m. The particles are initialized with the classic Sod shocktube⁸¹ conditions. The velocity is set

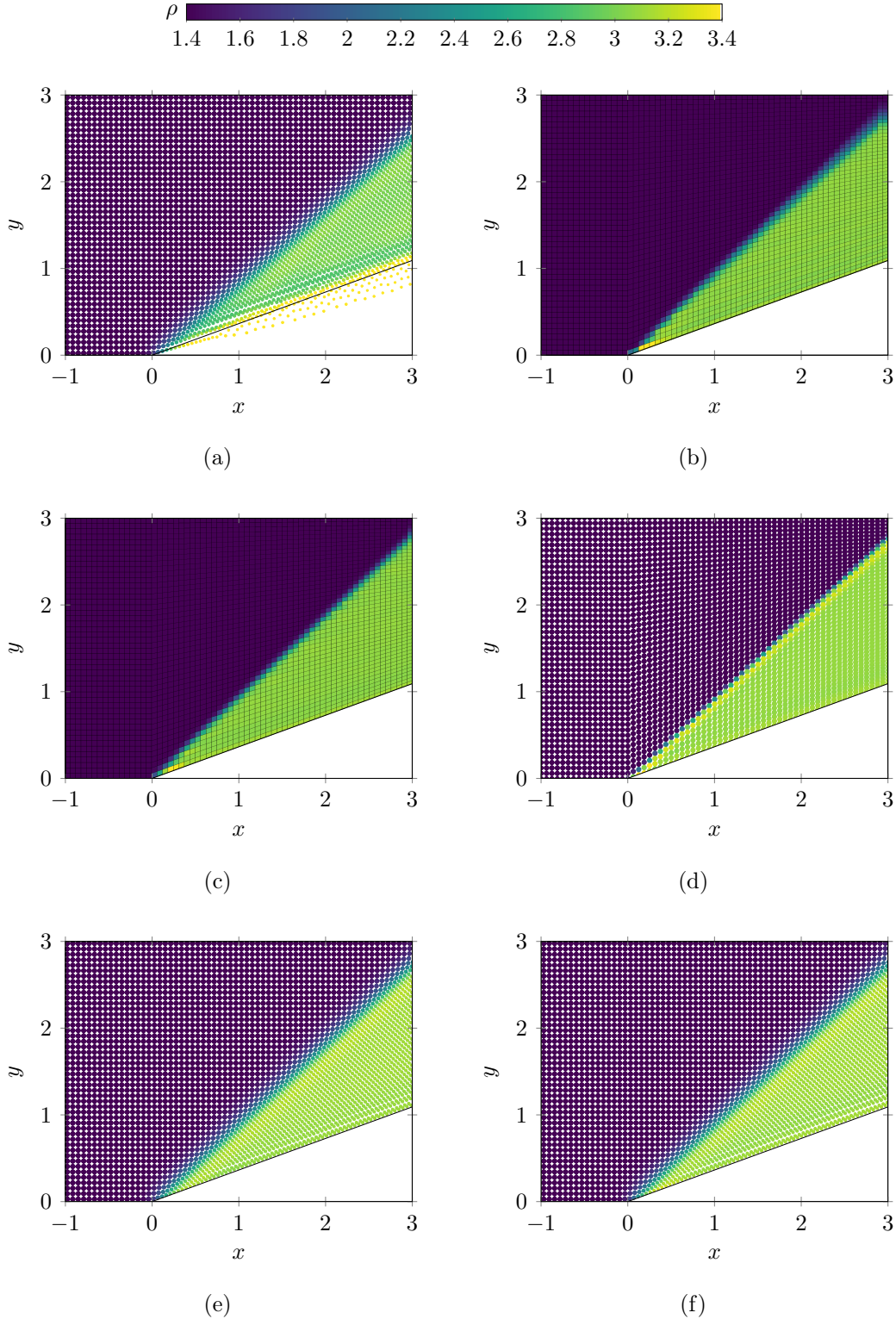


FIG. 2. Points/cells colored by density for the compression corner problem simulated using various methods/tools. (a) SPH with original Adami *et al.*⁹'s method. (b) First Order Upwind Roe. (c) Eilmer. (d) SU2. (e) SPH with present method, without ghost-mirror. (f) SPH with present method, with ghost-mirror.

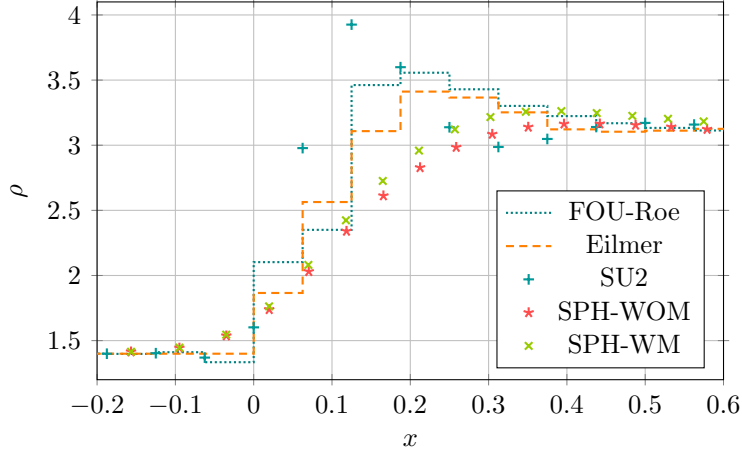


FIG. 3. Density along the wall about the corner.

M	γ	θ	β_{th}	$\beta_{\text{EC}}(\% \text{ error})$	$\beta_{\text{WOM}}(\% \text{ error})$	$\beta_{\text{WM}}(\% \text{ error})$
5	1.4	10°	19.38°	$18.0^\circ(-7.10)$	$19.20^\circ(-0.90)$	$19.24^\circ(-0.69)$
5	1.4	15°	24.32°	$21.8^\circ(-10.37)$	$24.10^\circ(-0.91)$	$24.12^\circ(-0.81)$
5	1.4	20°	29.80°	$27.0^\circ(-9.40)$	$29.54^\circ(-0.86)$	$29.55^\circ(-0.83)$
5	1.4	25°	35.78°	$32.6^\circ(-8.89)$	$35.48^\circ(-0.84)$	$35.49^\circ(-0.82)$
2	1.4	10°	39.31°	$39.0^\circ(-0.80)$	$39.16^\circ(-0.38)$	$39.19^\circ(-0.32)$
5	1.3	20°	28.76°	$27.0^\circ(-6.11)$	$28.55^\circ(-0.73)$	$28.54^\circ(-0.74)$

TABLE I. Comparison of error in wave angle β for different configurations of compression corner problem. β_{th} is the wave angle obtained using oblique shock theory⁸⁰. β_{EC} represents the values obtained by Englestad and Cassibry¹³ with their boundary treatment method. β_{WOM} and β_{WM} represent the values obtained using the methods from the present study, without ghost-mirrors and with ghost-mirrors, respectively.

as 0 m s^{-1} . Pressure and density are initialized as

$$\begin{bmatrix} \rho_L \\ p_L \end{bmatrix} = \begin{bmatrix} 1 \text{ kg m}^{-3} \\ 1 \text{ kg m}^{-3} \end{bmatrix}, \quad \begin{bmatrix} \rho_R \\ p_R \end{bmatrix} = \begin{bmatrix} 0.125 \text{ Pa} \\ 0.1 \text{ Pa} \end{bmatrix}, \quad (38)$$

where the subscripts L and R denote the left and right states. To avoid a spurious pressure blip, the quantities are smoothed about the initial discontinuity. This smoothed pressure of

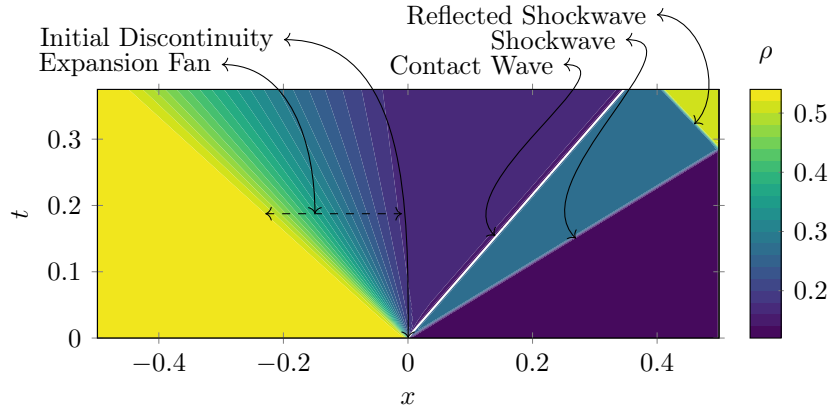


FIG. 4. xt -plot for reflecting shocktube.

a particle p_i can be expressed as

$$p_i = \frac{p_L - p_R}{1 + \exp\left(\frac{2(x_i - x_0)}{3\Delta x}\right)} + p_R, \quad (39)$$

where x_i is the x -component of its position vector, x_0 is the location of initial discontinuity and Δx is the particle spacing. Density is also smoothed, likewise. The simulation is run until the shockwave hits the right wall and reflects as shown in fig. 4. The walls at either end of the shock tube are dealt with using boundary treatment methods described in the present paper. The boundaries in the y -direction are set to be periodic. The periodicity is implemented internally in PySPH⁷³. The results in this section illustrate that the presented boundary treatment method works well with periodic boundaries.

The particle positions at $t = 0.375$ s colored by density are shown in fig. 5. The density profile is compared with the exact solution in fig. 6. The movement of particles results in the formation of a low particle density region around the contact discontinuity. It may also be noted that the contact discontinuity in fig. 6 appears smeared because of the smoothed initial condition and reduced particle density, largely due to the latter.

C. Hypersonic Cylinder

The bow shock formed upstream of a blunt cylinder-shaped body is usually examined as a standard test case for carbuncle instability. Mach 10 flow over the unit radius cylinder, ahead of a 14.04° cylinder cone is considered as shown in fig. 7. Particle spacing at the inlet is 0.025 m. The simulation is run till $t = 3.5$ s.

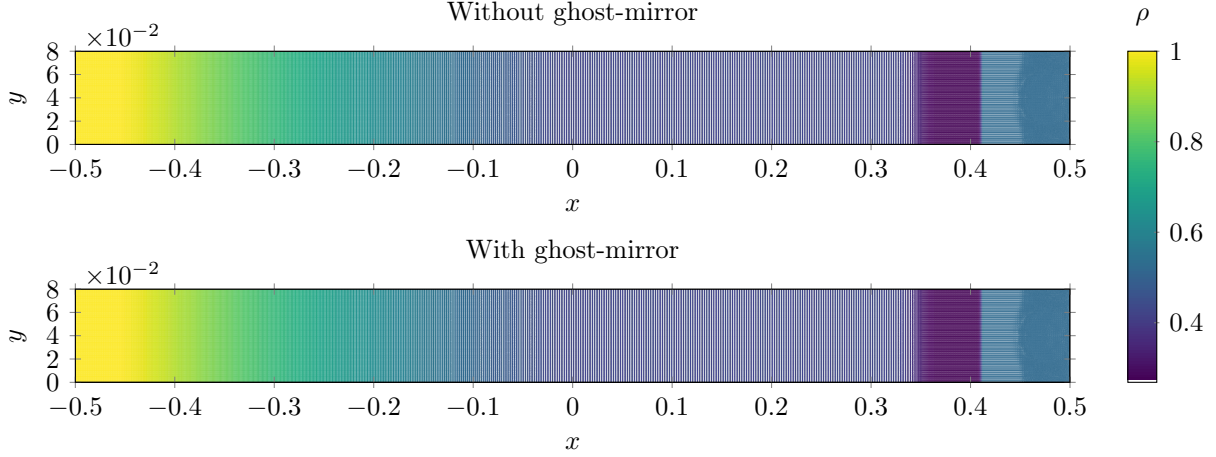


FIG. 5. Reflecting shocktube with particles colored by density.

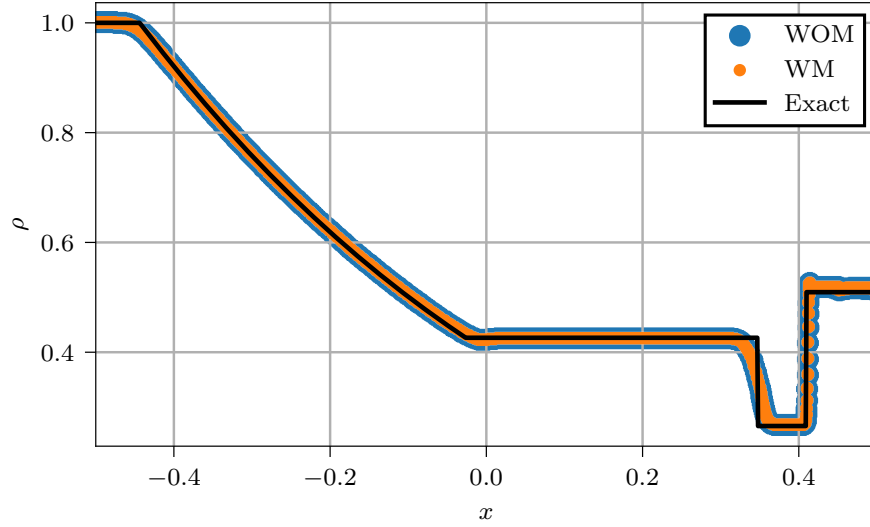


FIG. 6. Density variation with respect to exact for reflecting shocktube case

The shape of the shock front is modeled as a hyperbola, expressed as

$$x = R + \delta - R_C \cot^2 \beta \left[\left(1 + \frac{y^2 \tan^2 \beta}{R_c^2} \right)^{1/2} - 1 \right]. \quad (40)$$

Here, β is the wave angle for a the turn angle θ . The turn angle is 14.04° in this case. δ is the standoff distance, i.e. the shortest distance from the tip of the nose to the shockfront. R is the radius of the nose and R_C is the radius of curvature of shockwave at the vertex of the hyperbola. δ and R_C are correlated as

$$\frac{\theta}{R} = 0.386 \exp \left(\frac{4.67}{M_\infty^2} \right), \quad (41)$$

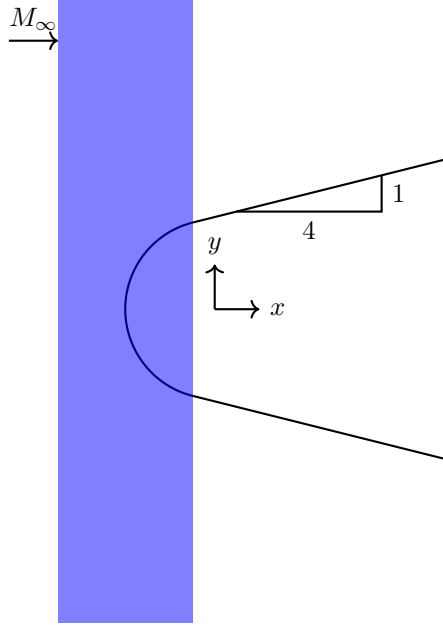


FIG. 7. Setup for hypersonic cylinder case. The flow domain is shaded blue.

and

$$\frac{\theta}{R} = 1.386 \exp \left[\frac{1.8}{(M_\infty - 1)^{0.75}} \right], \quad (42)$$

where M_∞ is the freestream Mach number. M_∞ is 10 in this case. The readers may also refer to the work of Billig⁸² or Anderson⁸³, chap. 5 for a more detailed explanation.

The shock front agrees fairly well with the profile given by eq. (40). Upon closer inspection, it may be observed that the curvature of the profile given by eq. (40) tends to exceed the simulation result, towards the outlet. However, plots presented by Billig⁸² are indicative of the fact that such minor variations can be expected. From fig. 8 it is quite clear that there is no evidence of carbuncle instability.

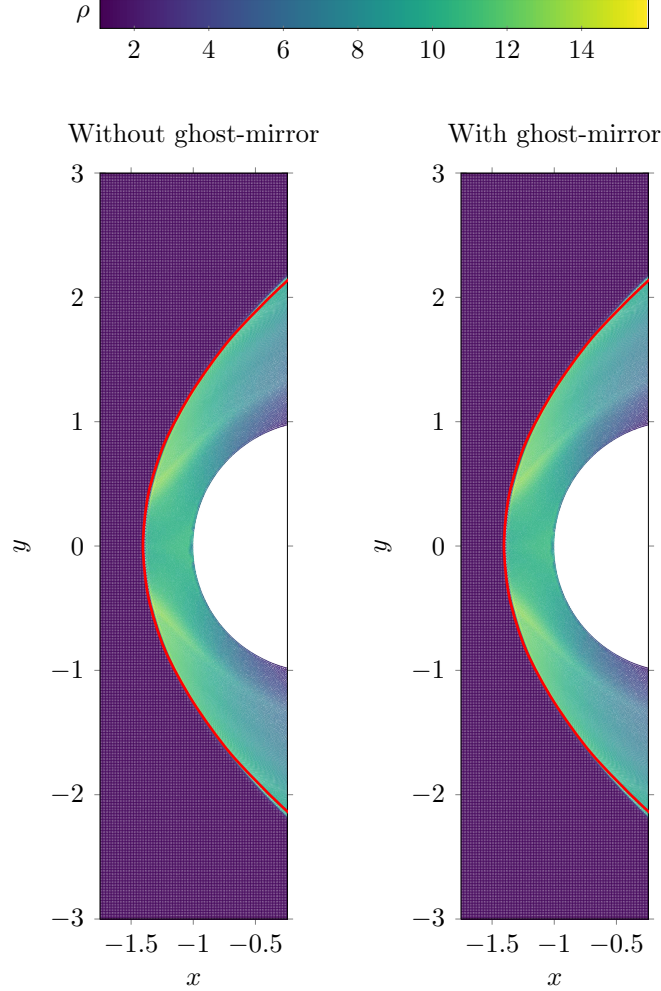


FIG. 8. Hypersonic cylinder with particles colored by density. The red line is the location of the shock front given by eq. (40).

D. Convergent Divergent Nozzle

This is a problem in which the transition from subsonic flow to supersonic flow is demonstrated. The nozzle profile can be obtained using

$$y = \begin{cases} y_0 & \text{if } x_0 \leq x \leq x_1 \\ \sqrt{R_{tu}^2 - (x - x_1)^2} & \text{if } x_1 < x \leq x_2 \\ R_{th} + R_{cu} - \sqrt{R_{cu}^2 - x^2} & \text{if } x_3 < x \leq x_4 \\ y_4 + (x - x_4) \tan(\theta) & \text{if } x_4 < x \leq x_5 \end{cases}. \quad (43)$$

The symbols in the above equation are to be read along with the markings in fig. 9. This profile is obtained from examples in the Eilmer repository, which in turn is a simplified

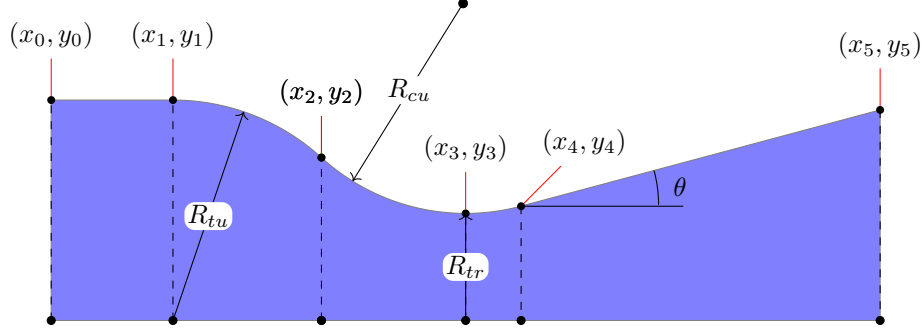


FIG. 9. Profile of convergent-divergent nozzle. Here, $R_{tu} = 1.5955$, $R_{tr} = 0.755$, $R_{cu} = 1.55$, $x_0 = -3$, $x_1 = 0.0$, $x_5 = 3$. These dimensions are in inches. $\theta = 15^\circ$.

adaption of the profile from the work of Back *et al.*⁸⁴. We simulate a rectangular, non-axisymmetric nozzle with this profile.

The particle spacing at the inlet is $R_{tu}/30$ inch. The simulation is run for 0.004 s. Air at temperature 300 K enters the inlet with a mass flux of 275.16 kg m^{-1} . For an isentropic quasi 1D convergent-divergent nozzle, the area ratio and Mach number are related as

$$\frac{A}{A_{tr}} = \left(\frac{\gamma + 1}{2} \right)^{-\frac{\gamma+1}{2(\gamma-1)}} \frac{\left(1 + \frac{\gamma-1}{2} M^2 \right)^{\frac{\gamma+1}{2(\gamma-1)}}}{M} \quad (44)$$

where A denotes area and A_{tr} is the area at the throat. The Mach number at the inlet can be obtained using the area ratio of the inlet to the throat. The velocity, density and pressure at the inlet are determined using this information.

From fig. 10, it can be observed that there are no qualitatively discernable differences between the two variants, just like the previous cases. From fig. 11 it can also be seen that the results are in agreement with a simulation performed using Eilmer. There is some difference very near the exit. This could be due to the exit boundary treatment method. It should be noted that the particle density at the exit for the SPH simulation is significantly lesser than the cell density near the exit for the mesh used in the Eilmer simulation.

E. Forward Facing Step

This problem deals with the flow of gas at Mach 3 over a forward-facing step in a duct^{85,86}. This problem is considered challenging due to the complex flow physics involved, including the formation interaction and reflection of waves. The computational domain is 3 m long and 1 m wide. A step of height 0.2 m is present at 0.6 m away from the inlet. The initial

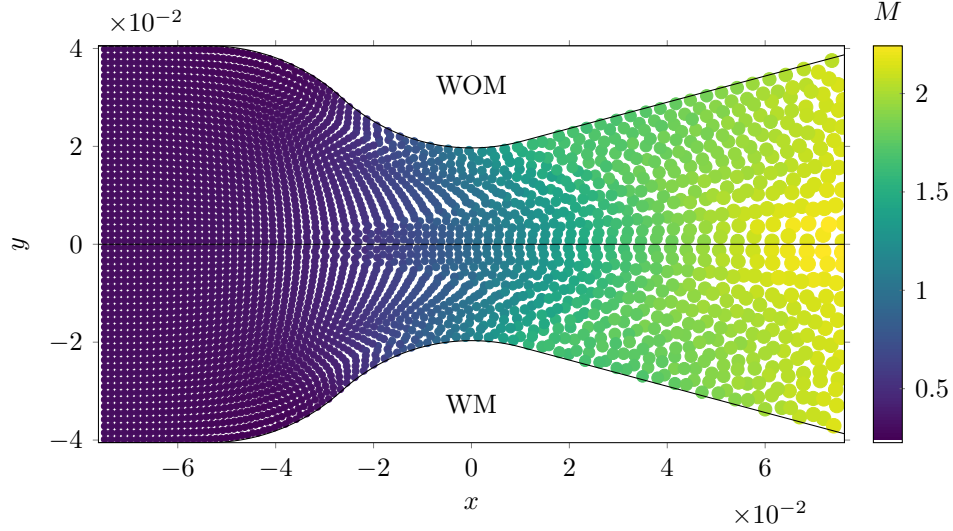


FIG. 10. Convergent-divergent nozzle with particles colored by local Mach number. The top and the bottom halves represent the result with and without ghost-mirror respectively.

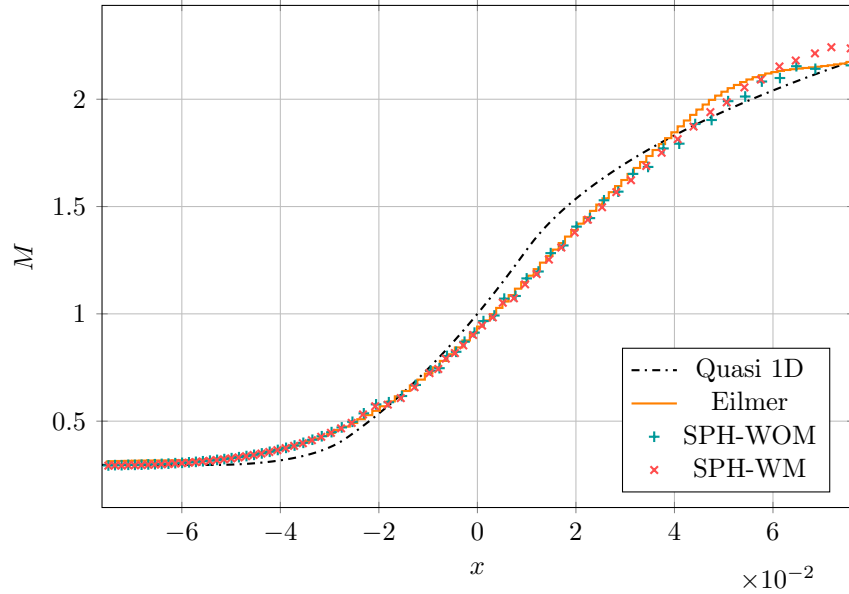


FIG. 11. Convergent divergent nozzle center line local Mach number.

particle spacing is 0.0125 m. Fluid enters the domain with density $\rho = 1.4 \text{ kg m}^{-3}$, velocities $u = 3.0 \text{ m/sec}$, $v = 0.0 \text{ m/sec}$, and pressure $p = 1.0 \text{ Pa}$. The simulation is run till $t = 2 \text{ s}$. As the flow evolves from the initial condition, we observe that a bow shock develops ahead of the step. The curvature of the bow reduces and it strikes the top wall. The curvature continues to reduce and the location of incidence on the top wall keeps moving upstream. Eventually, a triple point is formed and the Mach stem keeps traveling upstream. Meanwhile, the reflected

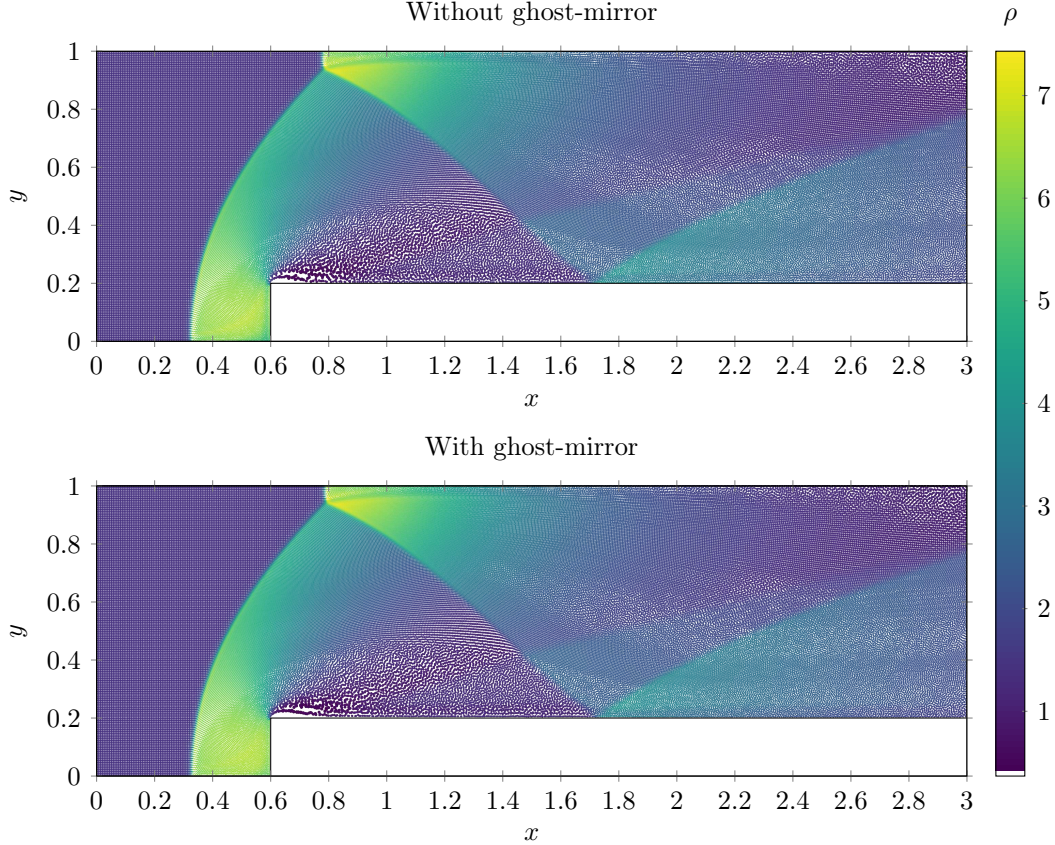


FIG. 12. Forward facing step with particles colored by density.

shock wave interacts with the expansion wave from the step-corner, strikes the bottom wall and reflects further.

The resulting shock pattern at $t = 2$ s can be read from fig. 12. The Mach stem is observed to be about 0.04 m long and located at about $x = 0.78$ m. The reflected wavefront strikes the bottom wall at about $x = 1.71$ m. These are in good agreement with the results that are observed in the literature. This indicates that the wall boundaries treated using the methods proposed in this paper are able to reflect the shock waves well.

F. Double Mach Reflection

Double Mach Reflection problem was proposed by Woodward and Colella⁸⁶ inspired by experimental and numerical studies of reflections of planar shocks in the air from a wedge. This problem involves a Mach 10 shock impinging a rigid wall at an angle of 60° . The impingement results in the formation of a complex shock reflection structure. It is a self-

similar structure that grows in size as the shock propagates. This problem is considered a difficult case for most numerical methods. The work Gao *et al.*⁸⁷ is the only study that we know of, which simulates this problem with SPH. However, they do this within the Eulerian framework. As a result, they did not have to face many challenges that this problem brings when moving particles are considered.

This problem is set up with an initial particle spacing is 0.0125 m. The reflecting ramp lies along the bottom of the problem domain, beginning at $x_0 = 1/6$ m. The angle between the shock and the reflecting boundary of 60° . As discussed in section II A, the choice of permeable boundary treatment method restricts us from having an exact moving shock wave of Mach 10 prescribed on the top boundary. We resort to the alternate setup described by Tan and Shu⁸⁸, Vevik *et al.*⁸⁹. The undisturbed fluid ahead of the shock has a density of 1.4 kg m^{-3} and a pressure of 1 Pa. The simulation is run till $t = 0.2$ s.

Figure 13 shows the result of simulation without the use of ghost-mirrors. It can be seen that there is considerable noise around the primary slip line and some near-wall disturbance between $x = 1.5$ m and $x = 2.0$ m. The primary match stem appears to be severely kinked. The formation of spot-like structures can also be noted. These structures are generally observed at an interface where particles having different masses interact. This is a known problem with SPH⁵⁶. From fig. 14, it can be observed that when this problem is simulated with the use of ghost-mirrors, the issues are less severe but they are present nonetheless. It has been demonstrated that spot-like structures can be mitigated by applying mass diffusion-based fixes proposed by Read and Hayfield⁶¹, Prasanna Kumar and Patnaik⁹⁰. By using an adaptive particle splitting and merging procedure which borrows from Sun *et al.*¹⁴ and Haftu *et al.*⁶⁷ we have results that demonstrate that the kinked Mach stem, the near-wall disturbance and the spot-like structures can be very effectively mitigated. To avoid digression, we reserve the details of this procedure and the results for another article. The point of showing this example in the present work is to demonstrate that the boundary condition implementation is effective even in such cases with complex shock wall interactions and successfully prevents particle penetration.

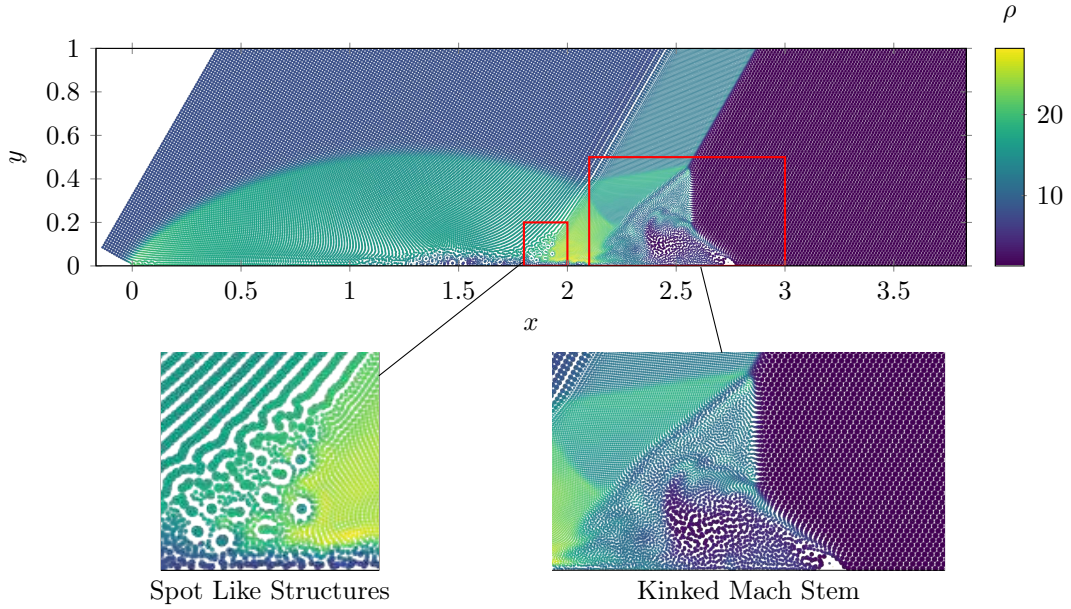


FIG. 13. Double Mach reflection simulated without ghost-mirror. The particles are colored by density.

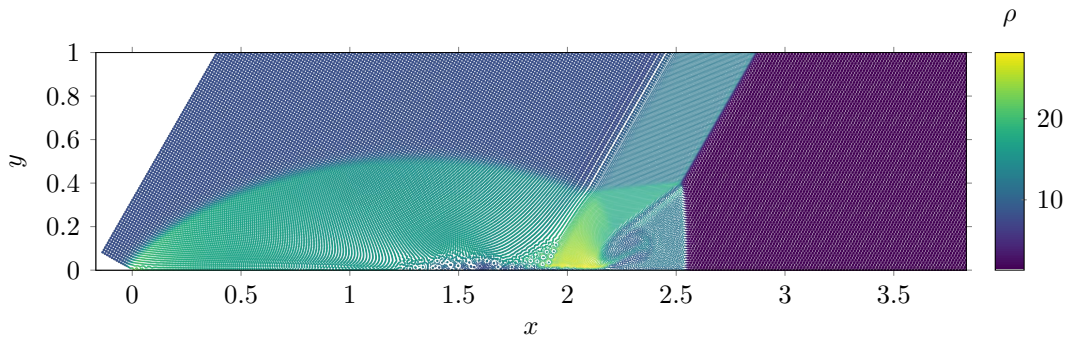


FIG. 14. Double Mach reflection simulated with ghost-mirror. The particles are colored by density.

G. Biconvex Aerofoil

This problem involves a biconvex aerofoil at 0° angle of attack in Mach 4.04 flow. A simple biconvex aerofoil with a chord, c_o of 1 m and a thickness-to-chord ratio is 0.1 is considered. The particle spacing at the inlet is 0.0125 m. The angle of attack is 0° . Freestream pressure, p_∞ , and density, ρ_∞ , are taken as 1 Pa and 1.4 kg m^{-3} respectively. The simulation is run till $t = 1 \text{ s}$.

Unlike most of the previously presented problems that demonstrate the strengths of SPH with the proposed boundary treatment method, this problem brings forward some

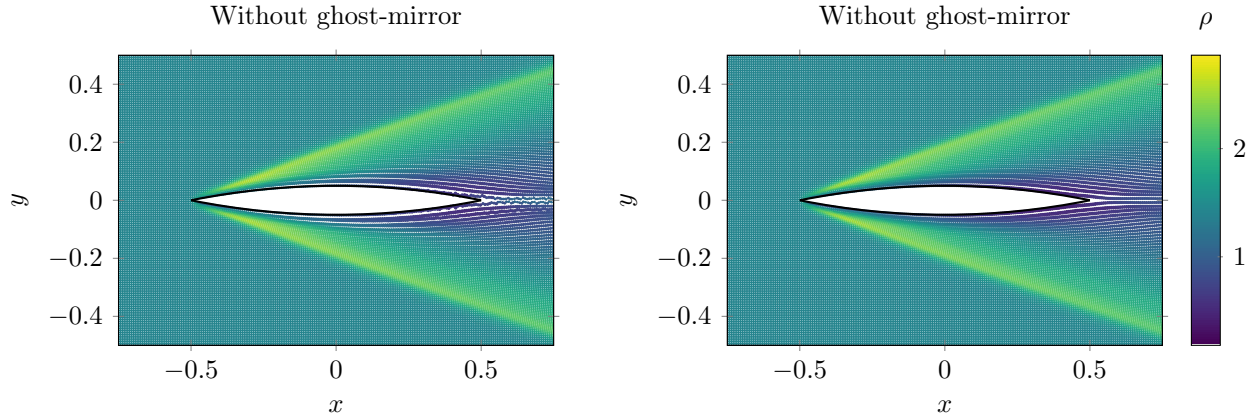


FIG. 15. Mach 4.04 flow over biconvex aerofoil at 0° angle of attack. The particle spacing at the inlet is 7×10^{-3} m. The particles are colored by density.

of the shortcomings. Meshes for geometries like these, that have sharp tips can be made to have high resolution at tips. However, we cannot achieve the same in SPH without an adaptive resolution procedure. Another issue is that the particles generated by the packing algorithm are not perfectly symmetric. The effect of lack of symmetry reduces with increasing resolution. So, we discretize the airfoil using ghost particles with a spacing that is half that of the fluid particles. We do not decrease the spacing further to keep the errors due to lack of consistency in the particle spacing about the interface, as discussed in section III E, in check.

The particle positions resulting from the simulation, colored by density, are shown in fig. 15. It was observed that the streak lines near the body are not static. The fluid particles close to the body become disordered as they pass by, differently based on the boundary treatment employed. The pressure over the body is shown in fig. 16a. Interpolation without the use of ghost-mirrors yields better results in this problem. It can be observed that the pressure over the aerofoil does not match perfectly with the inviscid theory. Along with the issues mentioned above, this could also be attributed to the usage of artificial viscosity. Despite all these issues, we can observe from fig. 16b that the results are convergent.

H. Rotating Square Projectile

This problem is also borrowed from the examples in the Eilmer repository. This problem involves a square projectile rotating about its center of mass in a Mach 6 flow. The side

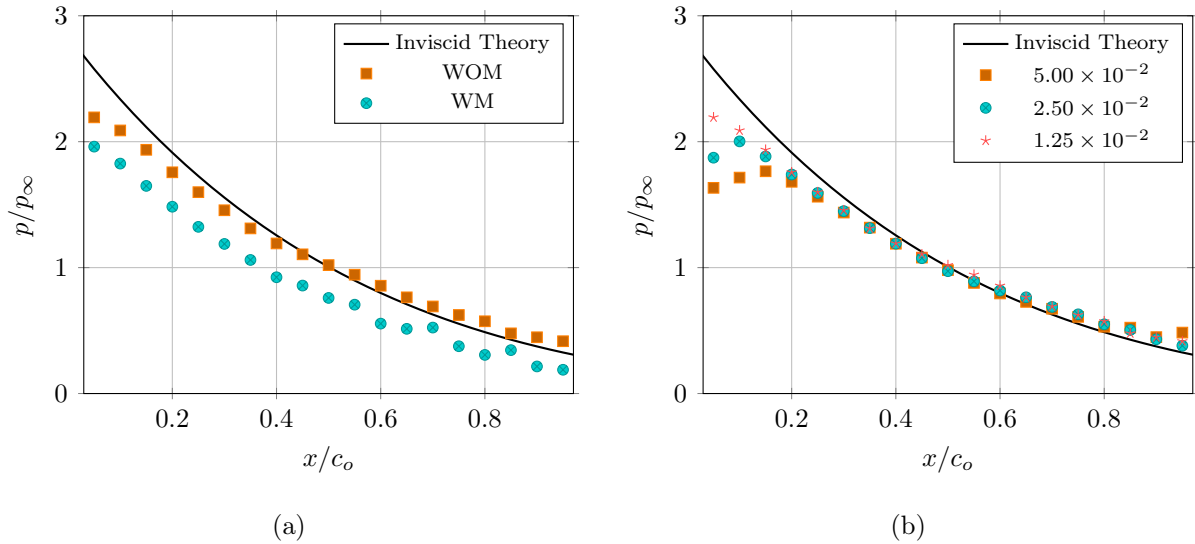


FIG. 16. Pressure on the upper surface of biconvex aerofoil. (a) Comparison of the with and without ghost-mirror variants at spacing 1.25×10^{-2} m. (b) Comparison of without ghost-mirror variant at different spacings.

of the square is 0.02 m. The initial particle spacing is 0.002 m. The freestream pressure, temperature and velocity are 760 Pa, 71 K and 1005.0 m s^{-1} respectively. The projectile is initially at rest and the angle of the square face relative to incoming flow, θ_0 is 0 rad. The rotation of the projectile is prescribed using angular velocity, ω as a function of time as

$$\omega(t) = A \cos\left(\frac{2\pi t}{t_f}\right), \quad (45)$$

where, A is the maximum angular velocity, 2000 rad s^{-1} and t_f is the final time, 2 ms.

In fig. 18, the bow shock formed in front of the projectile can be seen. From fig. 19a it can be observed that the force exerted on the projectile is in agreement with the results obtained using Eilmer. The mesh used for simulation with Eilmer is shown in fig. 17. Figure 19b shows that the force exerted on the projectile is not crippled by the penetration shield. It can be seen that the force is marginally less noisy when the penetration shield is used.

I. Apollo Reentry Capsule 3D

For this problem, the geometry of the Apollo reentry capsule is adapted from the work of Moss *et al.*⁹¹ and is shown in fig. 20. This problem aims to estimate the coefficient of

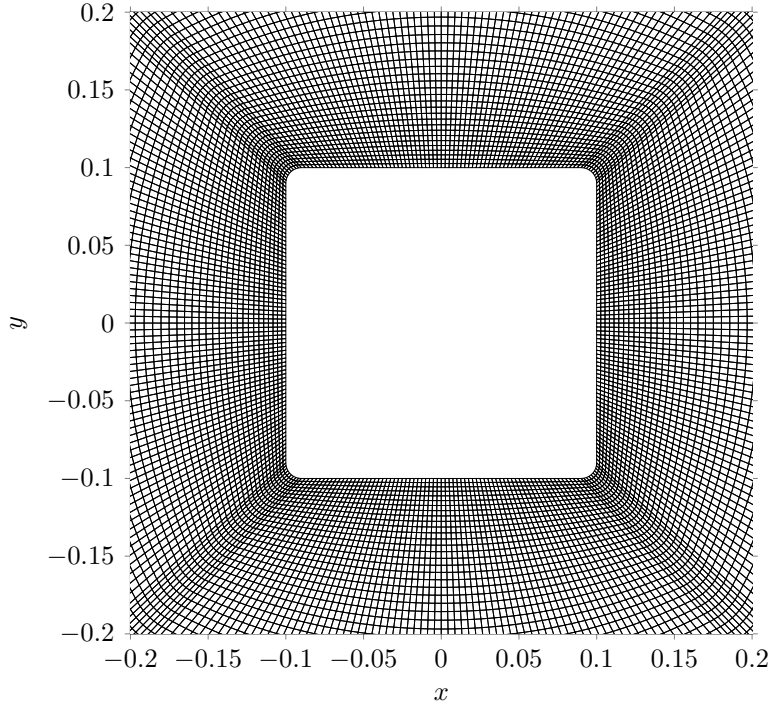


FIG. 17. Mesh around the rotating square projectile body for Eilmer.

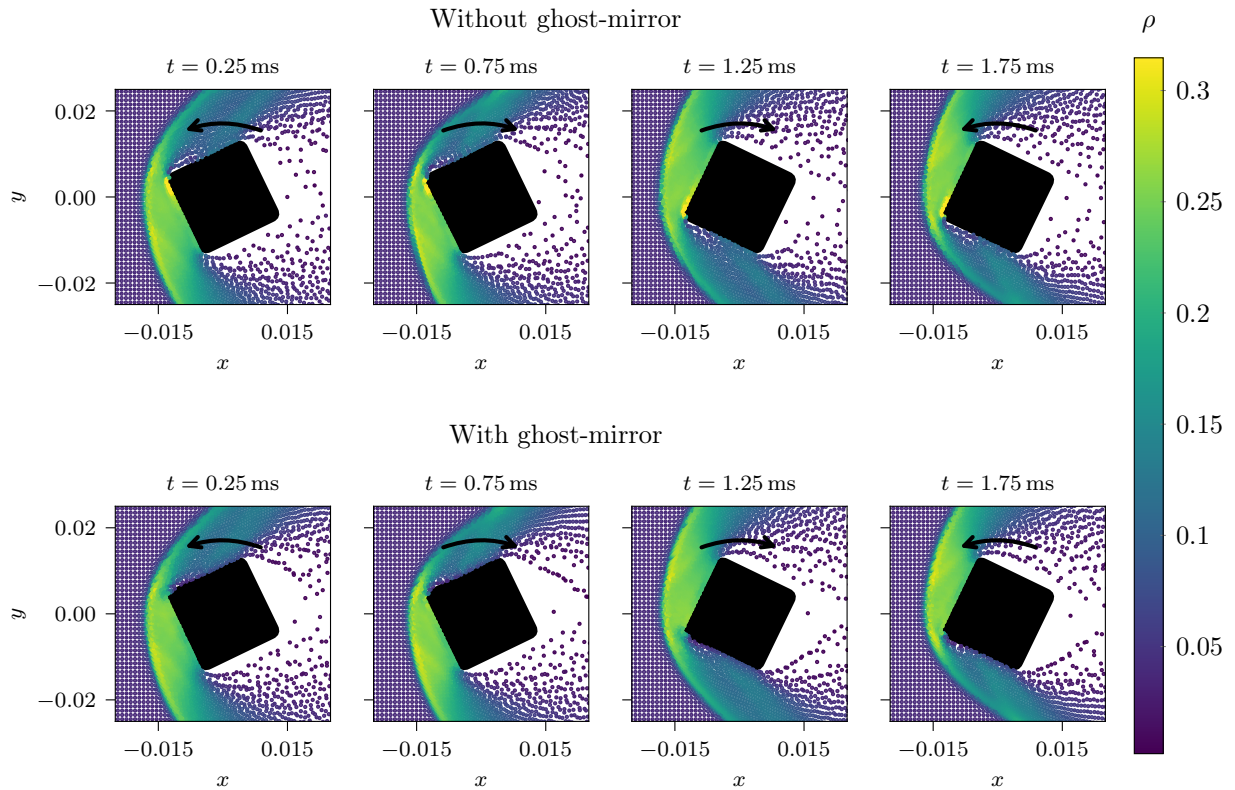


FIG. 18. Time snapshots showing particles colored by density for rotating square projectile problem.

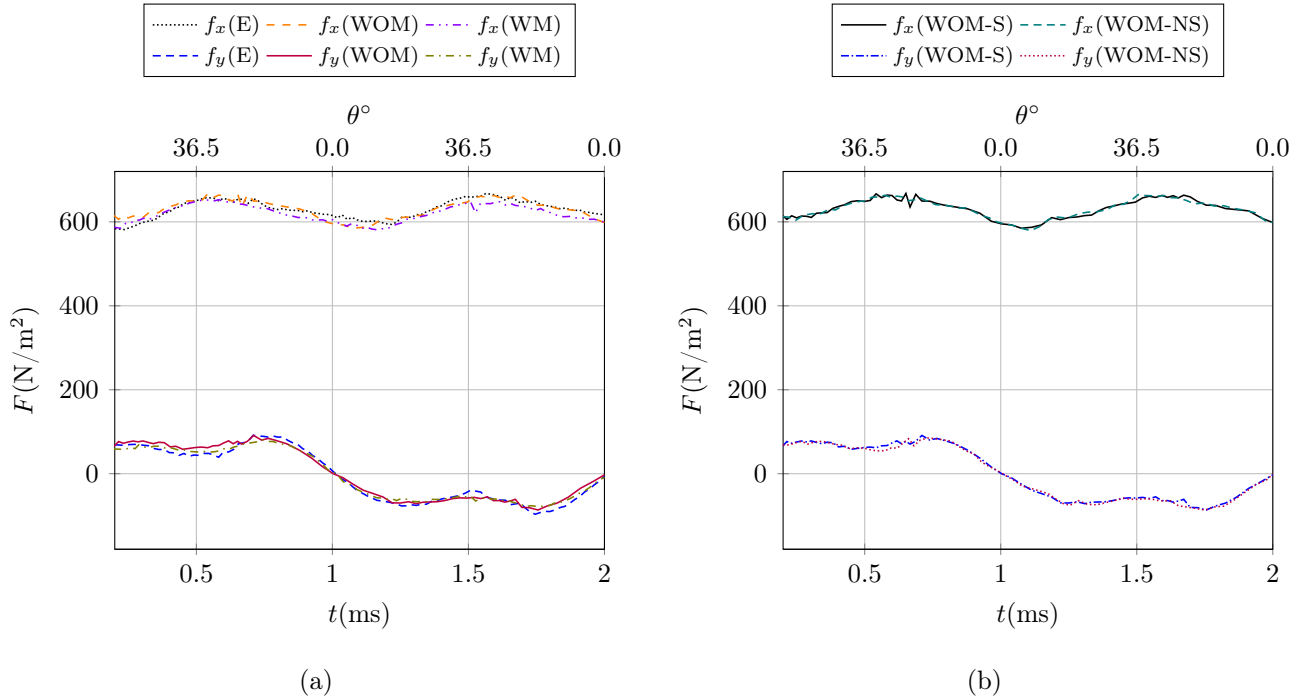


FIG. 19. Comparison of force on the rotating square projectile. (a) Comparison against Eilmer. The E in the legend stands for Eilmer. (b) Comparison of force with and without shield. The S and NS in the legend stand for Shield and No-Shield, respectively.

drag of the body, in order to demonstrate that SPH can be used for real-world 3D problems with the present boundary treatment method.

The streamwise direction is along the x -axis. The center of the forebody coincides with the origin. The inlet and outlet are 2 m upstream and 6 m downstream of the origin respectively. Both y and z extents of the domain are ± 8 m. The body is at 0° angle of attack. The flow enters the domain at Mach 2.5 with stagnation pressure and temperature of 1.2×10^6 Pa and 285 K respectively. The simulation is run until $t = 0.15$ s. For SPH simulations, the particle spacing at the inlet is 0.1 m.

For comparison, a similar setup is created in Eilmer. The details of the multi-block mesh can be read from fig. 21. The cell sizes vary, however, the body-fitted cell sizes are roughly 0.05 m, with double the resolution at the shoulder. The aftmost end is highly refined due to the constraint imposed by the corresponding foremost block.

To describe the nature of resolution independence, the expected observation is for the coefficient of drag to converge to a value as the resolution is increased. Now, the particle spacing could not have been much greater than 0.1 m as it would obliterate some of the

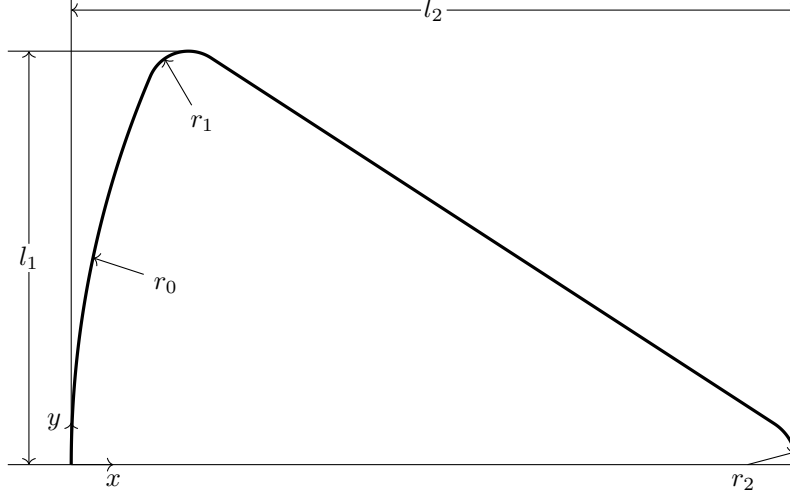
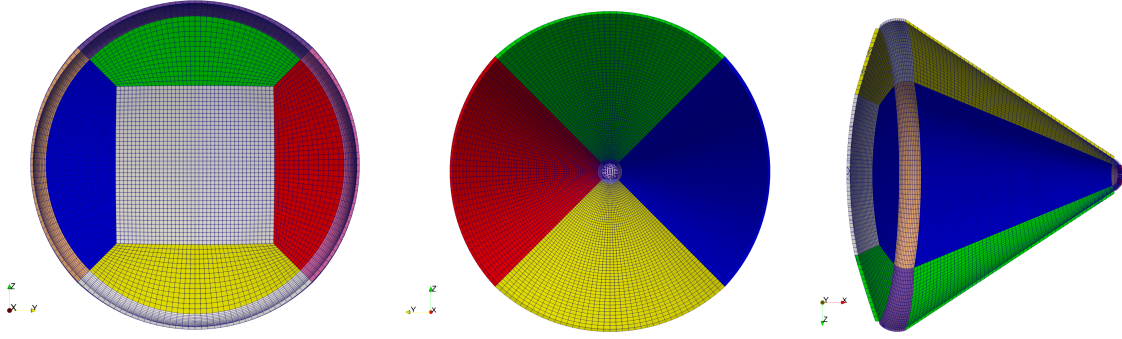


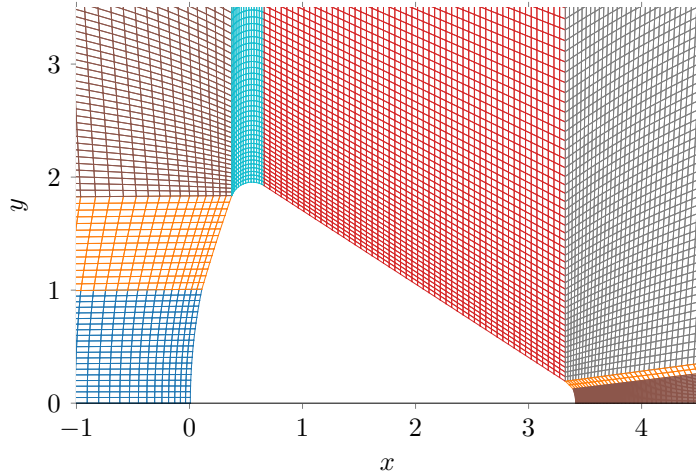
FIG. 20. Schematic of the Apollo reentry capsule. The dimensions are: $l_1=1.9558$ m, $l_2=3.4306$ m, $r_0=4.6939$ m, $r_1=0.2311$ m, $r_2=0.1956$ m.

relatively sharp curves on the body. Also, the particle spacing could not have been much smaller than the chosen spacing as that would have led to a prohibitively huge simulation time, given our computational capabilities. This ruled out the possibility of a resolution independence study. With that in account, the coefficient of drag is computed for the two variants of the proposed boundary treatment method and Eilmer is presented in table II. It needs to be noted that the estimation of forces in this kind of problem may require very fine resolutions. We do not have a common yardstick to specify the resolution and compare the results of SPH and FVM. With the result in table II, we would only like to drive the fact that results are not too far off, despite the inability to equate the resolution and our present inability to demonstrate resolution independence.

The density field for the two variants of the proposed boundary treatment method and Eilmer are shown in fig. 22. The SPH results are shown on a 500×250 grid. SPLASH⁹² interpolation procedure was used for this. It is observed that a separation bubble is formed behind the shoulder. These low-density regions are very resolution deficient in the SPH results. Despite the difference in drag, the point of showing this case is to once again demonstrate that the boundary treatment method can be used on practical three-dimensional geometries.



(a)



(b)

FIG. 21. Mesh for Apollo reentry capsule simulation with Eilmer. (a) Fore aft and side views of the body-fitted multiblock mesh, left to right. (b) Slice of multiblock mesh around the body.

Case	C_D
SPH without ghost-mirror	1.55
SPH with ghost-mirror	1.51
Eilmer	1.42

TABLE II. Coefficient of drag for the Apollo reentry capsule.

V. SUMMARY

We proposed boundary treatment methods for compressible SPH after identifying the challenges that are unique to compressible SPH. The issues highlighted in section III E are more pronounced in compressible scenarios. However, we expect that the proposed

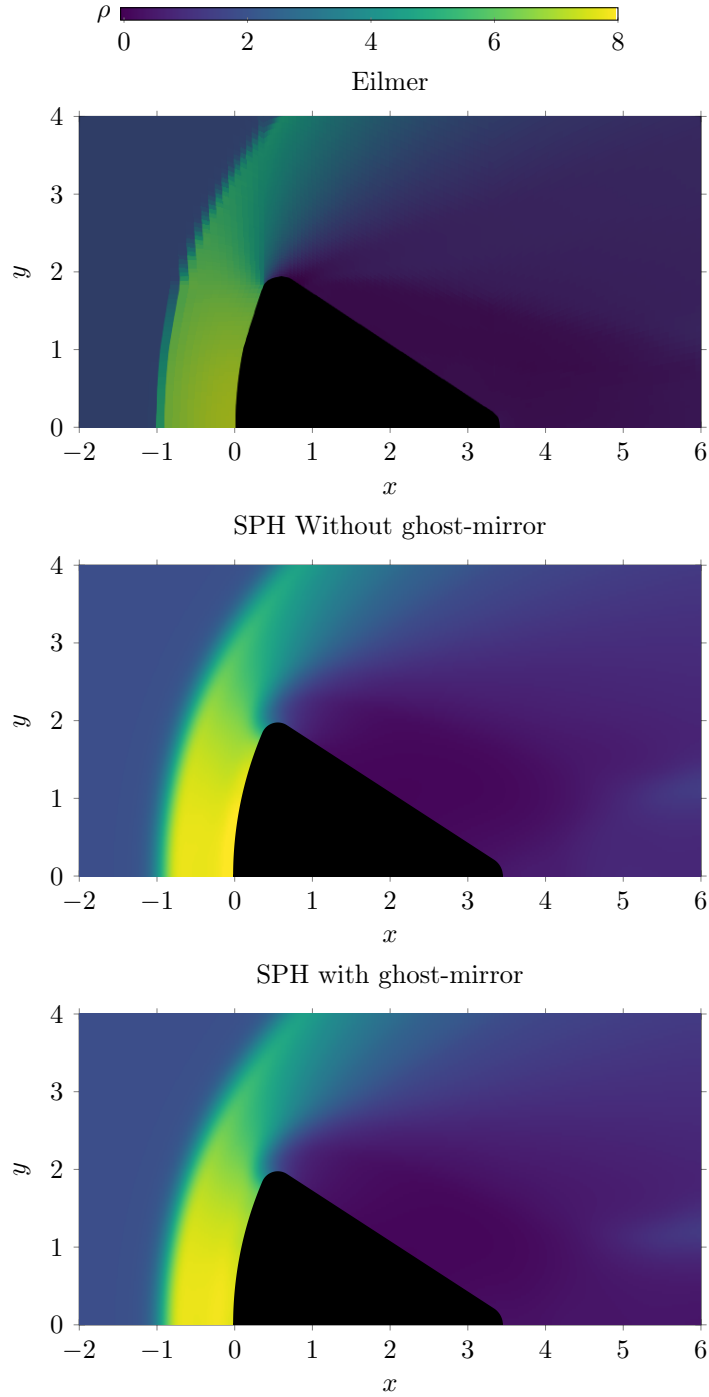


FIG. 22. Apollo reentry capsule results with cells colored by density.

remedies would be effective in incompressible scenarios as well. We were able to demonstrate significant improvements over the state-of-the-art¹³. The proposed boundary treatment methods do not add much complexity to the existing boundary treatment methods that are used in ISPH and WCSPH. The penetration shield which makes use of the TVF elegantly

prevents the particles from penetrating the boundary, without resorting to the usage of short-range forces at the boundary.

By and large, the results from both the extrapolation variants are comparable. It can be observed from table I that extrapolation with ghost-mirror generally result in marginally lower errors and does well in most cases except in the presence of sharp corners. The double mach reflection is a problem where extrapolation with ghost-mirrors clearly produces better results. However, the particle sparsity in wakes or separation bubbles can cause the ghost-mirrors to end up lacking neighbors. Consequently, the correction matrix for calculating W_{ij}^{LC} may be ill-formed, especially when the ratio of smoothing length to spacing is low. Extrapolation without ghost-mirrors can be regarded as more robust due to this pitfall.

The proposed methods are shown to be effective on a diverse set of problems of increasing complexity, many of which have not been simulated with SPH before to the best of our knowledge. The compression corner (section IV A) showcases a simple stationary oblique shock, reflecting shocktube (section IV B) showcases the reflection of a moving normal shock from a wall, hypersonic cylinder (section IV C) showcases a stationary bow shock in hypersonic flow, convergent divergent nozzle (section IV D) showcases subsonic to supersonic transition, and forward facing step (section IV E) showcases complex shockwave reflections and interactions. All these problems demonstrate acceptable results. The double Mach reflection (section IV F) showcases a complex shockwave interaction involving complex hypersonic shocks. The observed artifacts can be resolved by incorporating an adaptive refinement and derefinement procedure which we will discuss in a forthcoming article. The biconvex aerofoil (section IV G) showcases flow over a slender body with sharp tips. The results are convergent and improvement is likely with an adaptive refinement and derefinement procedure. The rotating square projectile (section IV H) showcases flow over a moving geometry. The results are in good agreement Eilmer⁷⁷. The Apollo reentry capsule (section IV I) showcases applicability in 3D. The results are promising despite the resolution deficiency. This summarizes the problem-wise results.

VI. FUTURE DIRECTIONS AND CONCLUDING REMARKS

We note that there is still ample room for improvement and the following are interesting problems that appear to be worthy of immediate attention:

- A better and faster packing algorithm for initializing ghost particles especially with variable resolution.
- Incorporation of particle splitting and merging procedure, so that more challenging real-world problems can be simulated.
- A shock-friendly particle shifting technique.
- A possible strategy for the fusion of the two extrapolation variants so that extrapolation is done without ghost-mirrors in the presence of sharp tips or voids, and with mirrors elsewhere.

We do not employ aggressive problem-specific tuning, chasing the absolute best results possible. So, individual problems may still have room for improvement. Our objective was just to show that the methods proposed in this paper have wide applicability, and perform well even without any problem-specific tuning. We have made an effort to mention all the intricacies involved. Additionally, we have provided the source at <https://gitlab.com/pypr/compressible-sph-bc> for the readers to study the actual implementation if they wish to. In the interest of reproducibility, all SPH results shown in this manuscript may be reproduced using an automation framework⁷⁵.

While mesh-based methods are known to be more mature and have better support for high-order schemes, meshless methods also possess some inherent indisputable advantages. For instance, with SPH, one, two or three-dimensional problems can be simulated with minimal changes to the code. FVM codes do not have this luxury. The Lagrangian nature also accords important benefits⁹³. For example, in the present work, the rotating square projectile problem illustrated that flows involving moving bodies can be simulated in SPH by merely updating ghost particles that represent the body. Mesh-based methods warrant more complicated procedures for the same.

If one excludes the time required to set the problem up and considers only the runtime, the presented SPH simulations would register as slower than their FVM counterparts. However, with FVM the quality of results is heavily dependent on the quality of the grid. The grid generation step in mesh-based methods requires a significant amount of time, operator skill, and effort. Therefore, with an automated particle packing algorithm for initializing ghost particles representing the body, we believe that the presented boundary treatment

methods take SPH a step closer to being an appealing alternative approach to mesh-based methods for engineering simulations involving compressible flows, especially when rapid results with minimal effort is a priority.

ACKNOWLEDGMENTS

The authors acknowledge the use of the computing resources of the ACE facility, Department of Aerospace Engineering, IIT Bombay.

REFERENCES

- ¹S. Rosswog, “Astrophysical Smooth Particle Hydrodynamics,” *New Astronomy Reviews* **53**, 78–104 (2009).
- ²V. Springel, “Smoothed Particle Hydrodynamics in Astrophysics,” *Annual Review of Astronomy and Astrophysics* **48**, 391–430 (2010).
- ³H. Takeda, S. M. Miyama, and M. Sekiya, “Numerical Simulation of Viscous Flow by Smoothed Particle Hydrodynamics,” *Progress of Theoretical Physics* **92**, 939–960 (1994).
- ⁴J. P. Morris, P. J. Fox, and Y. Zhu, “Modeling Low Reynolds Number Incompressible Flows Using SPH,” *Journal of Computational Physics* **136**, 214–226 (1997).
- ⁵A. Colagrossi and M. Landrini, “Numerical simulation of interfacial flows by smoothed particle hydrodynamics,” *Journal of Computational Physics* **191**, 448–475 (2003).
- ⁶M. Yildiz, R. A. Rook, and A. Suleman, “SPH with the multiple boundary tangent method,” *International Journal for Numerical Methods in Engineering* **77**, 1416–1438 (2009).
- ⁷F. Macia, M. Antuono, L. M. Gonzalez, and A. Colagrossi, “Theoretical Analysis of the No-Slip Boundary Condition Enforcement in SPH Methods,” *Progress of Theoretical Physics* **125**, 1091–1121 (2011).
- ⁸S. Marrone, M. Antuono, A. Colagrossi, G. Colicchio, D. Le Touzé, and G. Graziani, “ δ -SPH model for simulating violent impact flows,” *Computer Methods in Applied Mechanics and Engineering* **200**, 1526–1542 (2011).
- ⁹S. Adami, X. Hu, and N. Adams, “A generalized wall boundary condition for smoothed particle hydrodynamics,” *Journal of Computational Physics* **231**, 7057–7075 (2012).

- ¹⁰S. Marrone, A. Colagrossi, M. Antuono, G. Colicchio, and G. Graziani, “An accurate SPH modeling of viscous flows around bodies at low and moderate Reynolds numbers,” *Journal of Computational Physics* **245**, 456–475 (2013).
- ¹¹M. Antuono, C. Pilloton, A. Colagrossi, and D. Durante, “Clone particles: A simplified technique to enforce solid boundary conditions in SPH,” *Computer Methods in Applied Mechanics and Engineering* **409**, 115973 (2023).
- ¹²M. Silla and V. Bertola, “SPH simulation of oblique shocks in compressible flows: SPH Simulation of Oblique Shocks,” *International Journal for Numerical Methods in Fluids* **84**, 494–505 (2017).
- ¹³T. J. Englestad and J. T. Cassibry, “Investigations of a novel boundary condition approach for the accurate prediction of hypersonic oblique shocks in mesh-free Lagrangian simulations,” *Aerospace Science and Technology* **107**, 106322 (2020).
- ¹⁴P.-N. Sun, D. Le Touzé, G. Oger, and A.-M. Zhang, “An accurate SPH Volume Adaptive Scheme for modeling strongly-compressible multiphase flows. Part 1: Numerical scheme and validations with basic 1D and 2D benchmarks,” *Journal of Computational Physics* **426**, 109937 (2021).
- ¹⁵S. Adami, X. Hu, and N. Adams, “A transport-velocity formulation for smoothed particle hydrodynamics,” *Journal of Computational Physics* **241**, 292–307 (2013).
- ¹⁶P. Negi and P. Ramachandran, “How to train your solver: Verification of boundary conditions for smoothed particle hydrodynamics,” *Physics of Fluids* **34**, 117125 (2022).
- ¹⁷M. Lastiwka, M. Basa, and N. J. Quinlan, “Permeable and non-reflecting boundary conditions in SPH,” *International Journal for Numerical Methods in Fluids* **61**, 709–724 (2009).
- ¹⁸I. Federico, S. Marrone, A. Colagrossi, F. Aristodemo, and M. Antuono, “Simulating 2D open-channel flows through an SPH model,” *European Journal of Mechanics - B/Fluids* **34**, 35–46 (2012).
- ¹⁹A. Tafuni, J. M. Domínguez, R. Vacondio, and A. J. C. Crespo, “A versatile algorithm for the treatment of open boundary conditions in Smoothed particle hydrodynamics GPU models,” *Computer Methods in Applied Mechanics and Engineering* **342**, 604–624 (2018).
- ²⁰P. Negi, P. Ramachandran, and A. Haftu, “An improved non-reflecting outlet boundary condition for weakly-compressible SPH,” *Computer Methods in Applied Mechanics and Engineering* **367**, 113119 (2020).
- ²¹D. W. Holmes and P. Pivonka, “Novel pressure inlet and outlet boundary conditions for

- Smoothed Particle Hydrodynamics, applied to real problems in porous media flow,” *Journal of Computational Physics* **429**, 110029 (2021).
- ²²S. Zhang, W. Zhang, C. Zhang, and X. Hu, “A Lagrangian free-stream boundary condition for weakly compressible smoothed particle hydrodynamics,” *Journal of Computational Physics* **490**, 112303 (2023).
- ²³M. Ferrand, A. Joly, C. Kassiotis, D. Violeau, A. Leroy, F.-X. Morel, and B. D. Rogers, “Unsteady open boundaries for SPH using semi-analytical conditions and Riemann solver in 2D,” *Computer Physics Communications* **210**, 29–44 (2017).
- ²⁴B. Werdelmann, R. Koch, W. Krebs, and H.-J. Bauer, “An approach for permeable boundary conditions in SPH,” *Journal of Computational Physics* **444**, 110562 (2021).
- ²⁵J. Monaghan, “Simulating Free Surface Flows with SPH,” *Journal of Computational Physics* **110**, 399–406 (1994).
- ²⁶J. J. Monaghan and A. Kos, “Solitary Waves on a Cretan Beach,” *Journal of Waterway, Port, Coastal, and Ocean Engineering* **125**, 145–155 (1999).
- ²⁷J. Monaghan and J. Kajtar, “SPH particle boundary forces for arbitrary boundaries,” *Computer Physics Communications* **180**, 1811–1820 (2009).
- ²⁸P. M. Campbell, “Some New Algorithms for Boundary Value Problems in Smooth Particle Hydrodynamics,” Tech. Rep. DNA-TR-88-286 (Mission Research Corporation, 1720 Randolph Road, SE Albuquerque, NM 87106-4245, 1989).
- ²⁹J. C. Marongiu, F. Leboeuf, and E. Parkinson, “Numerical simulation of the flow in a Pelton turbine using the meshless method smoothed particle hydrodynamics: A new simple solid boundary treatment,” *Proceedings of the Institution of Mechanical Engineers, Part A: Journal of Power and Energy* **221**, 849–856 (2007).
- ³⁰M. R. Hashemi, R. Fatehi, and M. T. Manzari, “A modified SPH method for simulating motion of rigid bodies in Newtonian fluid flows,” *International Journal of Non-Linear Mechanics* **47**, 626–638 (2012).
- ³¹S. Kulasegaram, J. Bonet, R. W. Lewis, and M. Profit, “A variational formulation based contact algorithm for rigid boundaries in two-dimensional SPH applications,” *Computational Mechanics* **33**, 316–325 (2004).
- ³²J. Feldman and J. Bonet, “Dynamic refinement and boundary contact forces in SPH with applications in fluid flow problems,” *International Journal for Numerical Methods in Engineering* **72**, 295–324 (2007).

- ³³M. Ferrand, D. R. Laurence, B. D. Rogers, D. Violeau, and C. Kassiotis, “Unified semi-analytical wall boundary conditions for inviscid, laminar or turbulent flows in the meshless SPH method,” *International Journal for Numerical Methods in Fluids* **71**, 446–472 (2013).
- ³⁴A. Mayrhofer, B. D. Rogers, D. Violeau, and M. Ferrand, “Investigation of wall bounded flows using SPH and the unified semi-analytical wall boundary conditions,” *Computer Physics Communications* **184**, 2515–2527 (2013).
- ³⁵A. Leroy, D. Violeau, M. Ferrand, and C. Kassiotis, “Unified semi-analytical wall boundary conditions applied to 2-D incompressible SPH,” *Journal of Computational Physics* **261**, 106–129 (2014).
- ³⁶A. Mayrhofer, M. Ferrand, C. Kassiotis, D. Violeau, and F.-X. Morel, “Unified semi-analytical wall boundary conditions in SPH: Analytical extension to 3-D,” *Numerical Algorithms* **68**, 15–34 (2015).
- ³⁷L. Chiron, M. De Lefre, G. Oger, and D. Le Touzé, “Fast and accurate SPH modelling of 3D complex wall boundaries in viscous and non viscous flows,” *Computer Physics Communications* **234**, 93–111 (2019).
- ³⁸P. Boregowda and G.-R. Liu, “Insights on using the boundary integral SPH formulations to calculate Laplacians with Dirichlet boundaries,” *Engineering Analysis with Boundary Elements* **155**, 652–667 (2023).
- ³⁹A. Leroy, D. Violeau, M. Ferrand, L. Fratter, and A. Joly, “A new open boundary formulation for incompressible SPH,” *Computers & Mathematics with Applications* **72**, 2417–2432 (2016).
- ⁴⁰A. Ferrari, M. Dumbser, E. F. Toro, and A. Armanini, “A new 3D parallel SPH scheme for free surface flows,” *Computers & Fluids* **38**, 1203–1217 (2009).
- ⁴¹R. Vacondio, B. D. Rogers, and P. K. Stansby, “Smoothed Particle Hydrodynamics: Approximate zero-consistent 2-D boundary conditions and still shallow-water tests,” *International Journal for Numerical Methods in Fluids* **69**, 226–253 (2012).
- ⁴²G. Fournakos, R. Vacondio, and B. D. Rogers, “On the approximate zeroth and first-order consistency in the presence of 2-D irregular boundaries in SPH obtained by the virtual boundary particle methods,” *International Journal for Numerical Methods in Fluids* **78**, 475–501 (2015).
- ⁴³G. Fournakos, J. M. Dominguez, R. Vacondio, and B. D. Rogers, “Local uniform stencil (LUST) boundary condition for arbitrary 3-D boundaries in parallel smoothed particle

- hydrodynamics (SPH) models,” *Computers & Fluids* **190**, 346–361 (2019).
- ⁴⁴A. J. C. Crespo, M. Gómez-Gesteira, and R. A. Dalrymple, “Boundary Conditions Generated by Dynamic Particles in SPH Methods,” *Computers, Materials & Continua* **5**, 173–184 (2007).
- ⁴⁵B. Ren, M. He, P. Dong, and H. Wen, “Nonlinear simulations of wave-induced motions of a freely floating body using WCSPH method,” *Applied Ocean Research* **50**, 1–12 (2015).
- ⁴⁶N. Akinci, M. Ihmsen, G. Akinci, B. Solenthaler, and M. Teschner, “Versatile rigid-fluid coupling for incompressible SPH,” *ACM Transactions on Graphics* **31**, 1–8 (2012).
- ⁴⁷X. Liu, P. Lin, and S. Shao, “An ISPH simulation of coupled structure interaction with free surface flows,” *Journal of Fluids and Structures* **48**, 46–61 (2014).
- ⁴⁸X. Li, H. Zhang, and D. Yuan, “An Improved Dynamic Boundary Condition in SPH Method,” *Mechanics* **27**, 465–474 (2021).
- ⁴⁹A. English, J. M. Domínguez, R. Vacondio, A. J. C. Crespo, P. K. Stansby, S. J. Lind, L. Chiapponi, and M. Gómez-Gesteira, “Modified dynamic boundary conditions (mDBC) for general-purpose smoothed particle hydrodynamics (SPH): Application to tank sloshing, dam break and fish pass problems,” *Computational Particle Mechanics* **9**, 1–15 (2022).
- ⁵⁰M. E. Sikarudi and A. Nikseresht, “Neumann and Robin boundary conditions for heat conduction modeling using smoothed particle hydrodynamics,” *Computer Physics Communications* **198**, 1–11 (2016).
- ⁵¹J. Wang, W. Hu, X. Zhang, and W. Pan, “Modeling heat transfer subject to inhomogeneous Neumann boundary conditions by smoothed particle hydrodynamics and peridynamics,” *International Journal of Heat and Mass Transfer* **139**, 948–962 (2019).
- ⁵²A. Valizadeh and J. J. Monaghan, “A study of solid wall models for weakly compressible SPH,” *Journal of Computational Physics* **300**, 5–19 (2015).
- ⁵³P. W. Randles and L. D. Libersky, “Smoothed Particle Hydrodynamics: Some recent improvements and applications,” *Computer Methods in Applied Mechanics and Engineering* **139**, 375–408 (1996).
- ⁵⁴M. Antuono, A. Colagrossi, S. Marrone, and D. Molteni, “Free-surface flows solved by means of SPH schemes with numerical diffusive terms,” *Computer Physics Communications* **181**, 532–549 (2010).
- ⁵⁵D. J. Price, “Smoothed particle hydrodynamics and magnetohydrodynamics,” *Journal of Computational Physics* **231**, 759–794 (2012).

- ⁵⁶K. Puri and P. Ramachandran, “A comparison of SPH schemes for the compressible Euler equations,” *Journal of Computational Physics* **256**, 308–333 (2014).
- ⁵⁷P. Sun, A. Colagrossi, S. Marrone, M. Antuono, and A.-M. Zhang, “A consistent approach to particle shifting in the δ - Plus -SPH model,” *Computer Methods in Applied Mechanics and Engineering* **348**, 912–934 (2019).
- ⁵⁸D. Adepu and P. Ramachandran, “A corrected transport-velocity formulation for fluid and structural mechanics with SPH,” *Computational Particle Mechanics* (2023), [10.1007/s40571-023-00631-9](https://doi.org/10.1007/s40571-023-00631-9).
- ⁵⁹J. P. Morris and J. J. Monaghan, “A Switch to Reduce SPH Viscosity,” *Journal of Computational Physics* **136**, 41–50 (1997).
- ⁶⁰L. Cullen and W. Dehnen, “Inviscid smoothed particle hydrodynamics: Inviscid smoothed particle hydrodynamics,” *Monthly Notices of the Royal Astronomical Society* **408**, 669–683 (2010).
- ⁶¹J. I. Read and T. Hayfield, “SPHS: Smoothed particle hydrodynamics with a higher order dissipation switch: SPH with a higher order dissipation switch,” *Monthly Notices of the Royal Astronomical Society* **422**, 3037–3055 (2012).
- ⁶²S. Rosswog, “A Simple, Entropy-based Dissipation Trigger for SPH,” *The Astrophysical Journal* **898**, 60 (2020).
- ⁶³A. Khayyer, H. Gotoh, and Y. Shimizu, “A projection-based particle method with optimized particle shifting for multiphase flows with large density ratios and discontinuous density fields,” *Computers & Fluids* **179**, 356–371 (2019).
- ⁶⁴P. Rastelli, R. Vacondio, J. Marongiu, G. Fourtakas, and B. D. Rogers, “Implicit iterative particle shifting for meshless numerical schemes using kernel basis functions,” *Computer Methods in Applied Mechanics and Engineering* **393**, 114716 (2022).
- ⁶⁵P. Ramachandran and K. Puri, “Entropically damped artificial compressibility for SPH,” *Computers & Fluids* **179**, 579–594 (2019).
- ⁶⁶A. Muta and P. Ramachandran, “Efficient and accurate adaptive resolution for weakly-compressible SPH,” *Computer Methods in Applied Mechanics and Engineering* **395**, 115019 (2022).
- ⁶⁷A. Haftu, A. Muta, and P. Ramachandran, “Parallel adaptive weakly-compressible SPH for complex moving geometries,” *Computer Physics Communications* **277**, 108377 (2022).
- ⁶⁸M. Liu and G. Liu, “Restoring particle consistency in smoothed particle hydrodynamics,”

- Applied Numerical Mathematics* **56**, 19–36 (2006).
- ⁶⁹R. Vacondio, B. Rogers, P. Stansby, P. Mignosa, and J. Feldman, “Variable resolution for SPH: A dynamic particle coalescing and splitting scheme,” *Computer Methods in Applied Mechanics and Engineering* **256**, 132–148 (2013).
- ⁷⁰X. Yang and S.-C. Kong, “Adaptive resolution for multiphase smoothed particle hydrodynamics,” *Computer Physics Communications* **239**, 112–125 (2019).
- ⁷¹A. Muta, P. Ramachandran, and P. Negi, “An efficient, open source, iterative ISPH scheme,” *Computer Physics Communications* **255**, 107283 (2020), [arxiv:1908.01762](https://arxiv.org/abs/1908.01762).
- ⁷²P. Ramachandran, A. Muta, and M. Ramakrishna, “Dual-time smoothed particle hydrodynamics for incompressible fluid simulation,” *Computers & Fluids* **227**, 105031 (2021).
- ⁷³P. Ramachandran, A. Bhosale, K. Puri, P. Negi, A. Muta, A. Dinesh, D. Menon, R. Govind, S. Sanka, A. S. Sebastian, A. Sen, R. Kaushik, A. Kumar, V. Kurapati, M. Patil, D. Tavker, P. Pandey, C. Kaushik, A. Dutt, and A. Agarwal, “PySPH: A Python-based Framework for Smoothed Particle Hydrodynamics,” *ACM Transactions on Mathematical Software* **47**, 34:1–34:38 (2021).
- ⁷⁴P. Negi and P. Ramachandran, “Algorithms for uniform particle initialization in domains with complex boundaries,” *Computer Physics Communications* **265**, 108008 (2021).
- ⁷⁵P. Ramachandran, “Automan: A Python-Based Automation Framework for Numerical Computing,” *Computing in Science & Engineering* **20**, 81–97 (2018).
- ⁷⁶P. L. Roe, “Approximate Riemann solvers, parameter vectors, and difference schemes,” *Journal of Computational Physics* **43**, 357–372 (1981).
- ⁷⁷N. N. Gibbons, K. A. Damm, P. A. Jacobs, and R. J. Gollan, “Eilmer: An open-source multi-physics hypersonic flow solver,” *Computer Physics Communications* **282**, 108551 (2023).
- ⁷⁸T. D. Economou, F. Palacios, S. R. Copeland, T. W. Lukaczyk, and J. J. Alonso, “SU2: An Open-Source Suite for Multiphysics Simulation and Design,” *AIAA Journal* **54**, 828–846 (2016).
- ⁷⁹C. Geuzaine and J.-F. Remacle, “Gmsh: A 3-D finite element mesh generator with built-in pre- and post-processing facilities,” *International Journal for Numerical Methods in Engineering* **79**, 1309–1331 (2009).
- ⁸⁰J. D. Anderson, *Modern Compressible Flow: With Historical Perspective*, fourth edition ed. (McGraw Hill, New York, NY, 2021).

- ⁸¹G. A. Sod, “A Survey of Several Finite Difference Methods for Systems of Nonlinear Hyperbolic Conservation Laws,” *Journal of Computational Physics* **27**, 1–31 (1978).
- ⁸²F. S. Billig, “Shock-wave shapes around spherical-and cylindrical-nosed bodies.” *Journal of Spacecraft and Rockets* **4**, 822–823 (1967).
- ⁸³J. D. Anderson, *Hypersonic and High-Temperature Gas Dynamics, Third Edition* (American Institute of Aeronautics and Astronautics, Inc., Reston, VA, 2019).
- ⁸⁴L. H. Back, H. L. Gier, and P. F. Massier, “Comparison of measured and predicted flows through conical supersonic nozzles, with emphasis on the transonic region,” *AIAA Journal* **3**, 1606–1614 (1965).
- ⁸⁵A. F. Emery, “An evaluation of several differencing methods for inviscid fluid flow problems,” *Journal of Computational Physics* **2**, 306–331 (1968).
- ⁸⁶P. Woodward and P. Colella, “The numerical simulation of two-dimensional fluid flow with strong shocks,” *Journal of Computational Physics* **54**, 115–173 (1984).
- ⁸⁷T. Gao, T. Liang, and L. Fu, “A new smoothed particle hydrodynamics method based on high-order moving-least-square targeted essentially non-oscillatory scheme for compressible flows,” *Journal of Computational Physics* **489**, 112270 (2023).
- ⁸⁸S. Tan and C.-W. Shu, “Inverse Lax-Wendroff procedure for numerical boundary conditions of conservation laws,” *Journal of Computational Physics* **229**, 8144–8166 (2010).
- ⁸⁹U. S. Vevek, B. Zang, and T. H. New, “On Alternative Setups of the Double Mach Reflection Problem,” *Journal of Scientific Computing* **78**, 1291–1303 (2019).
- ⁹⁰S. S. Prasanna Kumar and B. S. V. Patnaik, “A multimass correction for multicomponent fluid flow simulation using Smoothed Particle Hydrodynamics,” *International Journal for Numerical Methods in Engineering* **113**, 1929–1949 (2018).
- ⁹¹J. Moss, C. Glass, and F. Greene, “DSMC Simulations of Apollo Capsule Aerodynamics for Hypersonic Rarefied Conditions,” in *9th AIAA/ASME Joint Thermophysics and Heat Transfer Conference* (American Institute of Aeronautics and Astronautics, San Francisco, California, 2006).
- ⁹²D. J. Price, “SPLASH: An Interactive Visualisation Tool for Smoothed Particle Hydrodynamics Simulations,” *Publications of the Astronomical Society of Australia* **24**, 159–173 (2007).
- ⁹³P. F. Hopkins, “A new class of accurate, mesh-free hydrodynamic simulation methods,” *Monthly Notices of the Royal Astronomical Society* **450**, 53–110 (2015).